Multi-fidelity probabilistic failure onset analysis of composite structures under uncertainties

Computer Methods in Applied Mechanics and Engineering 454 (2026) 118849

Contents lists available at ScienceDirect

Comput. Methods Appl. Mech. Engrg.

journal homepage: www.elsevier.com/locate/cma

Multi-fidelity probabilistic failure onset analysis of composite structures under uncertainties

D. Zamani, A. Pagani, M. Petrolo *, E. Carrera

MUL² Lab, Department of Mechanical and Aerospace Engineering, Politecnico di Torino, Corso Duca degli Abruzzi 24, 10129, Torino, Italy

ARTICLE INFO

Keywords:
Multi-fidelity modeling
Composite structures
Carrera unified formulation
Uncertainty analysis
Gaussian process regression
Adaptive learning

ABSTRACT

Advancements in composite manufacturing have enabled innovative design strategies to enhance stress distribution, stiffness, and overall performance of composite structures. However, uncertainties related to material variability, load fluctuations, and manufacturing defects continue to pose serious challenges for structural reliability and early failure prediction. This study presents a novel multi-fidelity probabilistic framework for analyzing composite laminates under uncertainties. The methodology integrates low- and high-fidelity structural theories generated via the Carrera Unified Formulation (CUF). An adaptive Gaussian Process Regression (GPR) model is employed to construct a probabilistic surrogate that selectively uses high-fidelity theories only where needed, based on uncertainty-driven learning. Compared to conventional Monte Carlo Simulations (MCS) based entirely on high-fidelity models, the proposed framework achieves comparable accuracy, with $R^2 > 0.99$ and nRMSE $< 1\%$, while reducing the computational cost by a factor of two to ten. Convergence is obtained with only 20–300 high-fidelity simulations, against 400–800 required by the reference benchmark. The approach is applied to a composite plate, a free-edge laminate, and an open-hole configuration, where the adaptive multi-fidelity model accurately captures through-thickness stresses and failure indices.

1. Introduction

Composite materials are widely utilized in aerospace structures due to their high strength-to-weight ratio, tailoring capabilities, and reliable mechanical performance under demanding loading conditions [1,2]. Although significant progress has been made in both research and industrial practice, the understanding of failure mechanisms in composites remains incomplete, particularly under uncertainties and progressive damage scenarios [3,4]. In these cases, predicting the probability of failure becomes particularly complex, forcing designers to use conservative safety factors [5,6], which diminishes the advantages of using composites as the final structures are penalised by excessive weight. Additionally, the inherent multiscale nature of these structures means that complex interactions at lower scales influence the structural response at the macroscale. This renders them particularly sensitive to uncertainties and their propagation across different scales (see [7–9]). Likewise, the use of automated techniques, such as Automated Fiber Placement (AFP), Automated Tape Laying (ATL), and Continuous Tow Shearing (CTS), can lead to manufacturing defects, which introduce uncertainties in their characterization ([10–12]). Defects include voids [13], resin-rich regions [14], ply waviness [15], fiber misalignments [16], and spatially varying fiber volume fractions [17], all of which can significantly alter local stiffness and strength, leading to unanticipated failure modes.

* Corresponding author.
E-mail addresses: dario.zamani@polito.it (D. Zamani), alfonso.pagani@polito.it (A. Pagani), marco.petrolo@polito.it (M. Petrolo), erasmo.carrera@polito.it (E. Carrera).

https://doi.org/10.1016/j.cma.2026.118849
Received 5 December 2025; Received in revised form 24 January 2026; Accepted 12 February 2026

Monte Carlo Simulation (MCS) is generally used as the reference for uncertainty quantification because of its ease of implementation and broad applicability; however, its slow convergence and the high computational cost due to the high number of evaluations needed can make it impractical in many engineering problems. Although advanced sampling techniques such as Latin Hypercube Sampling (LHS), Sobol- sequences, and importance sampling can improve efficiency, they do not overcome the inherent slow convergence rate of MCS when high-fidelity evaluations are costly [18,19]. These limitations motivate the necessity of surrogate modeling, such as Gaussian Process Regression (GPR) [20,21] for modeling the propagation of uncertainties. GPR is a probabilistic machine learning approach specifically designed for modeling complex systems when limited data are available. It is a non-parametric method that defines a probability distribution over all possible functions that fit the training data, capturing the underlying correlations in the data while providing predictions with quantified uncertainty, represented by the mean value and standard deviation. GPR can accurately model high-dimensional data even with small datasets, making it an efficient alternative to MCS. For example, GPR has been utilized to model the crystal growth kinetics in thermoplastic composites, capturing the interplay between diffusion and secondary nucleation during processing [22]. Additionally, in the context of damage and defect characterization, GPR has been instrumental in analyzing noisy datasets, providing reliable predictions even with limited experimental data [23,24]. An et al. [25] developed a Reliability-Based Design Optimization (RBDO) framework for composite laminates, integrating material property uncertainties and discrete-continuous delamination variables via a GPR-based surrogate model, which enabled stochastic evaluation by replacing costly Finite Element (FE) analyses within MCS. Bessa and Pellegrino [26] applied GPR to model the stochastic post-buckling behavior of ultra-thin composite shells, capturing the unstable response regime through a non-intrusive Bayesian framework. Similarly, Zhou et al. [27] proposed a framework for the analysis of curing-induced dimensional variability by creating a GPR surrogate for a high-fidelity, multi-scale FE model, enabling an efficient importance ranking of uncertain material parameters. Highlighting the need for robust predictive systems, Teimouri et al. [28] demonstrated the superior capability of GPR over conventional neural networks in handling manufacturing uncertainty; their work showed that a GPR model, trained exclusively on data from ideal nominal structures, could still accurately predict damage size and location in composite airfoils with stochastic ply thickness variations. In the domain of structural health monitoring, Paixão et al. [29] presented a damage quantification methodology where GPR established a probabilistic mapping between delamination regions and damage indices, with the index themselves being extracted from Lamb wave signals using auto-regressive models. Finally, to address the high cost of data acquisition, Yue et al. [30] developed an Adaptive Learning (AL) strategy specifically for Gaussian Process (GP) that incorporate multiple sources of uncertainty, and optimizing the selection of informative experimental samples for the shape control of large-scale composite structures.

In the framework of GPR, Multi-Fidelity (MF) models have proven to be effective tools for reducing computational costs while maintaining high accuracy, enabling the combination of models with different fidelities to achieve comparable results at a fraction of the cost of relying solely on High-Fidelity (HF) simulations. For example, Guo et al. [31] reduced the number of HF acquisitions by developing a hierarchical Kriging-based surrogate model that combines fine and coarse FE simulations to optimize variable-stiffness composites (VSC) [32]. Similarly, a GPR framework was developed by Garg et al. [33] which predicts the corrections required to improve the accuracy of an element's stiffness matrix, by upgrading it from the computationally cheap First-Order Shear Deformation Theory (FSDT) to the Higher-Order Zigzag Theory (HOZT). Expanding on this, An et al. [34] proposed a dynamic optimization framework that simultaneously considers the number of plies, layer thickness, and fiber orientations by employing a MF-GPR model. Their method effectively integrates Low-Fidelity (LF) coarse-mesh and HF fine-mesh FE simulations through an exponent-based correction strategy, enabling accurate and computationally efficient surrogate modeling across fidelity levels. An important aspect of constructing MF surrogates is the sampling strategy. In their work, Ribeiro et al. [35] focused on an adaptive sampling strategy, introducing alternative acquisition functions with variable fidelity: the Variable Fidelity Lower Confidence Bound (VF-LCB) and the Variable Fidelity Weighted Expected Improvement (VF-WEI). Unlike classical sampling methods, these functions provide explicit parameters that control the balance between exploration and exploitation, making it easier to integrate these models into optimization loops. Similarly, Tian et al. [36] proposed an Advanced Variance Reduction Method (EVRM) for reinforced shell optimization by applying the principles of MF to the sampling strategy itself. Their framework utilizes a LF model to determine the optimal variable pairing configurations, resulting in a more efficient HF training dataset for the final surrogate model. Furthermore, Li et al. [37] developed an adaptive clustering GPR framework for the real-time prediction of nonlinear structural responses. Their work demonstrated high accuracy in capturing complex nonlinear behaviours that could not be captured by uniform sampling methods alone, but required the use of adaptive sampling techniques.

In this work, the Carrera Unified Formulation (CUF) is adopted, enabling the generation of structural theories with different kinematic assumptions and fidelities within a single theoretical framework [38]. CUF allows the automatic generation of refined structural theories, including higher-order shear deformation and Layerwise (LW) descriptions, which are critical for capturing the anisotropic behavior of laminates under complex loading conditions [39,40]. The necessity of this hierarchical approach was further emphasized by Nali and Carrera [41], whose work confirmed that only refined LW models can accurately capture the through-the-thickness stress variations essential for failure analysis. De Miguel et al. [42] compared LW CUF with commercial 3D solid elements, demonstrating that refined LW CUF models achieve comparable accuracy in predicting 3D stress states and failure indices but with a significant reduction in computational cost. In this work, CUF is integrated with MF-GPR to provide accurate yet computationally efficient predictions of the 3D stess field and first-ply failure response under uncertainties.

This paper is structured as follows: Section 2 describes the formalism of the CUF for modeling composite laminates, emphasizing its capability to generate high- and low-fidelity models within a unified theoretical framework; Section 3 introduces the probabilistic machine learning framework based on GPR and the adaptive learning strategy employed to optimally select high-fidelity samples; Section 4 presents and discusses the results obtained using the proposed MF framework. Finally, Section 5 concludes the paper with a discussion of potential applications and future developments, particularly focusing on optimization under uncertainty.

2. Multi-fidelity structural theories using the Carrera Unified Formulation

In this study, composite laminates are analyzed using refined 2D models based on CUF [43], which was proven to deliver accurate results for a wide range of structural geometries and anisotropic material properties. Within the CUF framework, the three-dimensional displacement field is described by an arbitrary expansion in the thickness direction, $F_\tau(z)$, of the generalized displacement $\mathbf{u}_\tau$ that lay in the $x-y$ plane:

$$\mathbf{u}(x,y,z) = F_\tau(z)\mathbf{u}_\tau(x,y) \qquad \tau = 1,\dots,M \tag{1}$$

Following Einstein's notation, the subscript τ indicates summation over the M expansion terms. In this study, a Taylor Expansion (TE) is used to develop an Equivalent-Single-Layer (ESL) model. Conversely, a Lagrange Expansion (LE) is applied to individual layers to construct LW models [44]. To ensure continuity of displacements at the interfaces between layers, a displacement-based LW formulation with Lagrange expansion functions (LD) is adopted.

TE functions are hierarchical polynomials in the thickness coordinate z. For example, a second-order Taylor model is given by:

$$\begin{cases} u(x,y,z) = u_0(x,y) + u_1(x,y)\cdot z + u_2(x,y)\cdot z^2 \\ v(x,y,z) = v_0(x,y) + v_1(x,y)\cdot z + v_2(x,y)\cdot z^2 \\ w(x,y,z) = w_0(x,y) + w_1(x,y)\cdot z + w_2(x,y)\cdot z^2 \end{cases} \tag{2}$$

LE functions represent an alternative approach to defining through-the-thickness displacement approximations, particularly in high-order kinematic theories. Unlike TE, which use a global polynomial representation, LE discretize the thickness by introducing interpolation points at specific locations. This leads to a subdivision of the thickness into multiple local expansion domains, where the displacement field is approximated using Lagrange polynomials. The polynomial order is determined by the chosen set of interpolation functions. A third-order expansion is provided in Eq. (3):

$$\begin{cases} u(x,y,z) = u_1(x,y)\,F_1(z) + u_2(x,y)\,F_2(z) + u_3(x,y)\,F_3(z) + u_4(x,y)\,F_4(z), \\ v(x,y,z) = v_1(x,y)\,F_1(z) + v_2(x,y)\,F_2(z) + v_3(x,y)\,F_3(z) + v_4(x,y)\,F_4(z), \\ w(x,y,z) = w_1(x,y)\,F_1(z) + w_2(x,y)\,F_2(z) + w_3(x,y)\,F_3(z) + w_4(x,y)\,F_4(z), \end{cases} \tag{3}$$

Usually, to describe the Lagrange functions, it is preferred to use a natural reference system where the variable ξ is defined between -1 and $+1$. Eq. (4) reports the Lagrange functions related to the third-order expansion:

$$\begin{cases} F_1(\xi) = -\frac{9}{16}\left(\xi+\frac{1}{3}\right)\left(\xi-\frac{1}{3}\right)(\xi-1), & \xi_1 = -1, \\ F_2(\xi) = \frac{27}{16}(\xi-1)\left(\xi-\frac{1}{3}\right)(\xi+1), & \xi_2 = -\frac{1}{3}, \\ F_3(\xi) = -\frac{27}{16}(\xi+1)\left(\xi+\frac{1}{3}\right)(\xi-1), & \xi_3 = \frac{1}{3}, \\ F_4(\xi) = \frac{9}{16}\left(\xi+\frac{1}{3}\right)(\xi-1)\left(\xi-\frac{1}{3}\right), & \xi_4 = 1. \end{cases} \tag{4}$$

The notations TEn and LDn correspond to the use of Taylor and Lagrange polynomials of the nth order, respectively. Furthermore, XLDn specifies LW models employing X Lagrange polynomials of nth order per layer.

By integrating the FE method with CUF, the following expression for the three-dimensional displacement field is obtained:

$$\mathbf{u}(x,y,z) = N_i(x,y)F_\tau(z)\mathbf{q}_{\tau i} \quad i = 1,\dots,N_n \quad \tau = 1,\dots,M \tag{5}$$

in which $\mathbf{q}_{\tau i}$ denotes the unknowns vector, and N_n is the number of nodes in each element. The present study consideres bi-quadratic FE, referred to as Q9, as the $N_i(x,y)$ shape functions.

The governing equations are derived through the principle of virtual displacements (PVD). First, the principle underlying PVD is applied to describe the problem in terms of virtual work, i.e.,

$$\delta\mathcal{L}_{int} = \delta\mathcal{L}_{ext} \tag{6}$$

The virtual variation of the internal strain energy is defined as:

$$\delta\mathcal{L}_{int} = \int_V \delta\boldsymbol{\epsilon}^T\boldsymbol{\sigma}\,dV \tag{7}$$

where V is the volume of the body. The virtual work due to external loadings includes the contribution of surface loads, $\mathbf{P}_S$, line loads, $\mathbf{P}_l$, and point loads, $\mathbf{P}$; and can be written in the following form:

$$\delta\mathcal{L}_{ext} = \int_S \delta\mathbf{u}^T\mathbf{P}_S\,dS + \int_l \delta\mathbf{u}^T\mathbf{P}_l\,dl + \delta\mathbf{u}^T\mathbf{P} \tag{8}$$

Eq. (7) can be reformulated by employing Eq. (5), the constitutive equation $\boldsymbol{\sigma} = \mathbf{C}\boldsymbol{\epsilon}$, and the geometrical relations between strains and displacements, resulting in:

$$\delta\mathcal{L}_{int} = \delta\mathbf{q}_{sj}^T\left[\int_V \mathbf{D}^T(N_jF_s)\widetilde{\mathbf{C}}\mathbf{D}(N_iF_\tau)\,dV\right]\mathbf{q}_{\tau i} = \delta\mathbf{q}_{sj}^T\mathbf{k}^{ij\tau s}\mathbf{q}_{\tau i} \tag{9}$$

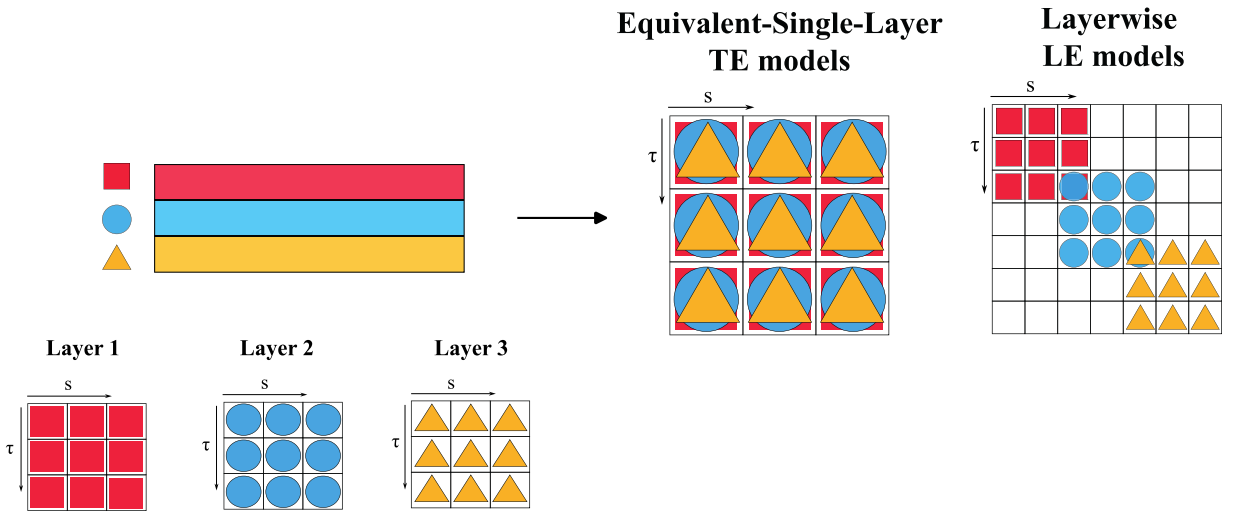

Fig. 1. Assembly of the stiffness matrix using an Equivalent-Single-layer and Layerwise approach.

in which $\mathbf{k}^{ij\tau s}$ is the 3×3 Fundamental Nucleus (FN) of the stiffness matrix, which is invariant regardless of the order of the $N_i(x, y)$ shape functions and the $F_\tau(z)$ expansion. The differential operator matrix containing the geometrical relations is expressed as $\mathbf{D}(\cdot)$. For orthotropic materials with a generic fiber orientation in space, the global components of the elasticity tensor $\widetilde{\mathbf{C}}$ are computed using the rotation matrix $\mathbf{T}$ without altering the definition of the FN. As described in [45], $\widetilde{\mathbf{C}}$ is the material stiffness matrix in the global reference frame, calculated as $\widetilde{\mathbf{C}} = \mathbf{T}\mathbf{C}\mathbf{T}^T$. Finally, the global assembled stiffness matrix $\boldsymbol{K}$ is constructed by iterating over the indices i, j, τ, and s. The assembly of the stiffness matrix, $\boldsymbol{K}$, varies based on the chosen modeling approach. Two commonly utilized strategies for analyzing multilayered structures are ESL and LW methods, as mentioned previously. In ESL modeling, the properties of individual layers are homogenized and then combined to compute the stiffness matrix. On the other hand, the LW method models each layer independently, expanding the displacement field within each lamina. These two assembly approaches are illustrated in Fig. 1 for a plate with three layers.

3. Probabilistic machine learning framework

3.1. Multi-fidelity surrogate with gaussian processes

This study employs a probabilistic machine learning framework to predict the three-dimensional stress distributions and the corresponding Hashin 3D failure indices through the laminate thickness under material and load uncertainties. The framework follows a MF approach and employs GPR to integrate simulations of varying fidelity. These models are systematically derived within the CUF framework, which serves as a generator of structural theories. For the LF models, ESL theories with a low-order TE (ESL-TE1/ESL-TE2) are used. These structural theories are the simplest models capable of capturing shear deformation effects. Specifically, ESL-TE1 is comparable to the classical FSDT. For the HF models, the LW approach with a first- or third-order LE (LW-LD1/LW-LD3) is used. Previous works [39,41] have shown that these models are essential for predicting the three-dimensional stress state, including transverse shear and out-of-plane normal components, even in thin-walled structures. The modeling strategy is shown in Fig. 2, which depicts the combination of in-plane Q9 FE with through-the-thickness expansions that define the model fidelity. This MF framework is designed to balance the computational efficiency of the ESL model with the high accuracy of the LW approach. The ability of the LW approach to capture detailed layer responses is critical for accurately describing failure onset in anisotropic structures (see [42]).

This study addresses uncertainties from two primary sources: material properties and applied loads. Variability in the elastic and strength properties is modeled to represent common manufacturing defects, such as fiber misalignments [46,47], voids [48–50], and resin-rich zones [51,52]. These physical variations and load fluctuations are modeled as random variables with prescribed statistical distributions, in this work, normal or uniform. The uncertain input vector is defined as $\mathbf{x} \in \mathbb{R}^d$, where d denotes the number of random variables. Let $z \in [-h/2,\ h/2]$ be the spatial coordinate along the laminate thickness, as instance. A normalized thickness coordinate $\zeta = 2z/h \in [-1, 1]$ is then introduced and discretized over a fixed grid $\{\zeta_p\}_{p=1}^{P}$. For a given quantity of interest, $y(\mathbf{x}, \zeta)$ represents the scalar response evaluated through the thickness at coordinate ζ and for the input vector $\mathbf{x}$, such as a stress, displacement, or failure index. The low- and high-fidelity counterparts are indicated by $y_{LF}(\mathbf{x}, \zeta)$ and $y_{HF}(\mathbf{x}, \zeta)$:

$$\mathbf{y}_{LF}(\mathbf{x}) = \left[y_{LF}(\mathbf{x}, \zeta_1), \ldots, y_{LF}(\mathbf{x}, \zeta_P)\right]^T \in \mathbb{R}^P, \qquad \mathbf{y}_{HF}(\mathbf{x}) = \left[y_{HF}(\mathbf{x}, \zeta_1), \ldots, y_{HF}(\mathbf{x}, \zeta_P)\right]^T \in \mathbb{R}^P. \tag{10}$$

A nested sampling design is considered, with HF evaluations defined as a subset of the LF ones and placed at the same $(\mathbf{x}_n, \zeta_p)$ coordinates:

$$\mathcal{D}_L = \{(\mathbf{x}_n, \zeta_p)\}_{n,p}, \qquad \mathcal{D}_H = \{(\mathbf{x}_n, \zeta_p)\}_{n \in \mathcal{I}_H, p}, \qquad \mathcal{D}_H \subset \mathcal{D}_L, \tag{11}$$

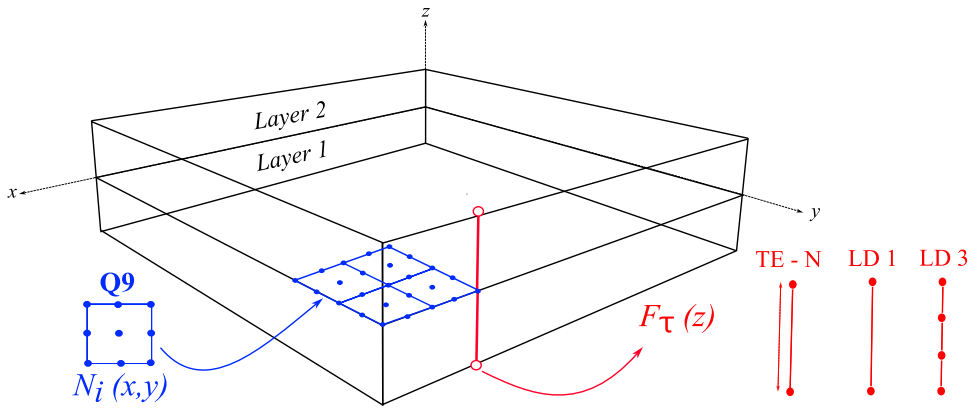

Fig. 2. Schematic of the CUF modeling strategy, showing the in-plane Q9 discretization and the through-the-thickness expansions defining the LF (ESL-TE-N) and HF (LW-LD1/LD3) models.

where D_L and D_H denote the sets of LF and HF samples, respectively. The index set $I_L = \{1, \dots, N_L\}$ corresponds to the LF input points, while $I_H \subset I_L$ identifies the HF subset. This guarantees well-posed LF/HF discrepancies at identical locations and reduces estimation variance in the MF coupling.

To make the framework more stable and easier to train, the model outputs are transformed using a smooth monotonic function $g(\cdot)$ [53–55]. This step helps the Gaussian Process (GP) handle highly nonuniform values, such as failure indices, which often exhibit strong asymmetry and a few peaks. Among several tested transformations, the inverse hyperbolic sine function (see Ref[56]) was found to be the most effective for this type of data:

$$g(y) = \operatorname{asinh}\left(\frac{y}{c}\right). \tag{12}$$

The function behaves almost linearly for small and moderate values, meaning that it does not distort the normal range of data, while it grows more slowly for large values. In this way, extremely high values have less influence on the regression, but the physical meaning and the sign of the data are preserved. For each output, the scaling constant c corresponds to the 90th percentile of the absolute HF data, keeping the majority of samples within the linear range of the transformation and reducing the effect of outliers. The GPR model is then trained on the warped data, and its predictions are transformed back to the original space using the inverse function, $g^{-1}(w) = c \cdot \sinh(w)$. The LF/HF discrepancy in the transformed space is then defined as:

$$\delta_g(\mathbf{x}, \zeta) = g\big(y_{HF}(\mathbf{x}, \zeta)\big) - g\big(y_{LF}(\mathbf{x}, \zeta)\big). \tag{13}$$

Let $\tilde{\mathbf{x}} = (\mathbf{x}, \zeta)$ and $\tilde{\mathbf{x}}' = (\mathbf{x}', \zeta')$ denote two generic input points defined by the design variables $\mathbf{x}$ and the normalized thickness coordinate ζ. The discrepancy is modeled as a GP, which defines a probability distribution over a collection of functions and is fully specified by a mean function $m(\tilde{\mathbf{x}})$ and a covariance function, also known as the kernel, $k_\theta(\tilde{\mathbf{x}}, \tilde{\mathbf{x}}')$ [57,58]. The model for the function is therefore expressed as:

$$\delta_g(\tilde{\mathbf{x}}) \sim \mathcal{GP}\big(m(\tilde{\mathbf{x}}),\ k_\theta(\tilde{\mathbf{x}}, \tilde{\mathbf{x}}')\big), \tag{14}$$

In this work, the structural response is dependent on both the uncertain parameters $\mathbf{x}$ and the spatial coordinate, such as the through-thickness position z. To model this, a separable kernel is employed, which factorizes the covariance into two components: one accounting for variations across the input parameters $\mathbf{x}$ and the other describing correlations along the thickness coordinate ζ. This decouples the influence of the physical parameters from the spatial dependency, as follows:

$$k_\theta(\tilde{\mathbf{x}}, \tilde{\mathbf{x}}') = k_{\text{par}}(\mathbf{x}, \mathbf{x}')\, k_{\text{sp}}(\zeta, \zeta'), \tag{15}$$

where both κ_{par} and κ_{sp} are Radial Basis Function (RBF) kernels [59,60]. The kernel for the input parameters, κ_{par}, incorporates Automatic Relevance Determination (ARD) [61–63], which assigns a unique length-scale parameter l_i to each input dimension:

$$k_{\text{par}}(\mathbf{x}, \mathbf{x}') = \sigma_f^2 \exp\left(-\frac{1}{2}\sum_{i=1}^{d}\frac{(x_i - x_i')^2}{\ell_i^2}\right), \tag{16}$$

Here, σ_f^2 is the signal variance and the vector $\mathbf{l} = [l_1, \dots, l_d]$ contains the length-scales. The inverse length-scales, $1/l_i$, provide a direct measure of the sensitivity of the model output to each input parameter. The ARD formulation is applied only to the parameter kernel, which deals with the stochastic input space and operates in a multidimensional domain where each uncertain parameter may exhibit a different level of influence on the response. In contrast, the spatial kernel acts on a single scalar coordinate through the thickness, for which an isotropic RBF formulation with a single length-scale is sufficient:

$$k_{\text{sp}}(\zeta, \zeta') = \sigma_\zeta^2 \exp\left(-\frac{(\zeta - \zeta')^2}{\ell_\zeta^2}\right) \tag{17}$$

Hyperparameters $\theta = \{\sigma_f^2, \{\ell_i\}_{i=1}^d, \sigma_\zeta^2, \ell_\zeta, \sigma_n^2\}$ are estimated by maximizing the log-marginal likelihood, defined as $\mathcal{L}(\theta) = \log p(\mathbf{y}_w \mid \tilde{\mathbf{X}}, \theta)$ [20,64,65]. Let $\tilde{\mathbf{X}} = \{\tilde{\mathbf{x}}_j\}_{j=1}^N$ be the set of N training inputs with $\tilde{\mathbf{x}}_j = (\mathbf{x}_j, \zeta_j)$, and let $\mathbf{y}_w = [\,\delta_g(\tilde{\mathbf{x}}_1), \ldots, \delta_g(\tilde{\mathbf{x}}_N)\,]^T$ collect the transformed discrepancies. Define $\mathbf{K} = K_\theta(\tilde{\mathbf{X}}, \tilde{\mathbf{X}}) + \sigma_n^2 \mathbf{I}$, where $K_\theta(\tilde{\mathbf{X}}, \tilde{\mathbf{X}}) \in \mathbb{R}^{N\times N}$ has entries $[K_\theta]_{ij} = k_\theta(\tilde{\mathbf{x}}_i, \tilde{\mathbf{x}}_j)$, $\mathbf{I}$ is the $N \times N$ identity matrix, $\mathbf{1} \in \mathbb{R}^N$ is the vector of ones, and σ_n^2 denotes the observation noise variance. A constant mean is used, $m(\cdot) \equiv \beta$.

$$\mathcal{L}(\theta) = \log p(\mathbf{y}_w \mid \tilde{\mathbf{X}}, \theta) = -\tfrac{1}{2}(\mathbf{y}_w - \beta\mathbf{1})^\top \mathbf{K}^{-1}(\mathbf{y}_w - \beta\mathbf{1}) - \tfrac{1}{2}\log|\mathbf{K}| - \tfrac{N}{2}\log(2\pi). \tag{18}$$

For any test point $\tilde{\mathbf{x}}_* = (\mathbf{x}_*, \zeta_*)$, with $\mathbf{k}_* = K_\theta(\tilde{\mathbf{x}}_*, \tilde{\mathbf{X}}) = [\,k_\theta(\tilde{\mathbf{x}}_*, \tilde{\mathbf{x}}_1), \ldots, k_\theta(\tilde{\mathbf{x}}_*, \tilde{\mathbf{x}}_N)\,]^T$, the posterior predictive mean and variance of the transformed discrepancy $\tilde{\mathbf{x}}$ are:

$$m_*(\tilde{\mathbf{x}}_*) = \beta + \mathbf{k}_*^\top \mathbf{K}^{-1}(\mathbf{y}_w - \beta\mathbf{1}), \tag{19}$$

$$s_*^2(\tilde{\mathbf{x}}_*) = k_\theta(\tilde{\mathbf{x}}_*, \tilde{\mathbf{x}}_*) - \mathbf{k}_*^\top \mathbf{K}^{-1}\mathbf{k}_*. \tag{20}$$

The MF prediction in the physical space is obtained by correcting the LF at the same input and inverting the initial domain transformation:

$$\hat{y}_{MF}(\mathbf{x}_*, \zeta_*) = g^{-1}\Big(g\big(y_{LF}(\mathbf{x}_*, \zeta_*)\big) + m_*(\mathbf{x}_*, \zeta_*)\Big). \tag{21}$$

To represent aleatory uncertainty, a LHS set $\{\mathbf{x}^{(i)}\}_{i=1}^{N_s} \sim p(\mathbf{x})$ is propagated through the MF surrogate using only the GP posterior mean. For each input sample $\mathbf{x}^{(i)}$ and for each through-thickness coordinate ζ_p:

$$\hat{y}_{MF}^{(i)}(\zeta_p) = g^{-1}\Big(g\big(y_{LF}(\mathbf{x}^{(i)}, \zeta_p)\big) + m_*(\mathbf{x}^{(i)}, \zeta_p)\Big). \tag{22}$$

The 90% Confidence Interval (CI) band, representing aleatory variability, is computed as the percentile envelope across the MF surrogate predictions:

$$\mathrm{CI}_{90\%}(\zeta_p) = \Big[\, Q_{0.05}\big\{\hat{y}_{MF}^{(i)}(\zeta_p)\big\}_i,\; Q_{0.95}\big\{\hat{y}_{MF}^{(i)}(\zeta_p)\big\}_i \,\Big] \tag{23}$$

where Q_α denotes the empirical α-quantile over the sample index i at fixed spatial location ζ_p. This approach separates the variability due to $p(\mathbf{x})$. The GP posterior variance s_*^2 (see Eq. (20)) quantifies surrogate epistemic uncertainty and is used as acquisition score in the adaptive selection of new HF samples.

3.2. Adaptive sampling for multi-fidelity surrogates

While the MF-GPR framework provides a robust structure for uncertainty propagation, its overall efficiency is critically dependent on the strategic placement of the limited and computationally expensive HF training points. A static, pre-defined Design of Experiments (DoE), such as an LHS, is often suboptimal [66]. It distributes the available HF evaluations uniformly across the parameter space, failing to concentrate sampling in regions of higher complexity or non-linearity where the discrepancy between the low- and high-fidelity models is most pronounced. To overcome this limitation, this work employs an Adaptive Learning (AL) strategy to intelligently and iteratively guide the selection of new HF data points [67,68]. Expected Improvement (EI) was first proposed as the standard acquisition technique for GP surrogates [69,70]. Later research expanded on this idea by using criteria based on information measures, improvement probabilities, or confidence bounds [71–74]. These approaches can all be seen as part of a spectrum of exploration and exploitation [75,76]: pure exploration looks for high-uncertainty regions but may overlook response structure [77], whereas pure exploitation targets low expected responses but runs the risk of premature convergence [78,79]. More efficient methods couple the GP posterior mean with its variance, combining the two to produce sample selections that lower uncertainty and increase predictive accuracy at the same time [80,81]. Maintaining the exploration-exploitation balance is critical in this study since high stress gradients, anisotropic effects, and non-uniform failure indices are frequently observed at free edges, and in proximity of open holes, and manufacturing flaws. As explained in Section 2, classical ESL theories are inadequate for multilayered structures as they overlook the C_z^0 requirements and violate local equilibrium at free surfaces and interfaces [82]. Multi-fidelity approaches improve these constraints by combining LF models, which capture global trends at a minimal cost, with strategically placed HF data to refine uncertainty estimates [83–85]. The limitations of LF models are most evident for quantities exhibiting strong through-thickness gradients, such as out-of-plane stresses, interlaminar shear, and delamination indices.

The AL process begins by defining a large, discrete master candidate pool, $\mathcal{U}_{\text{master}}$, from which all training points are subsequently drawn. This pool is generated using LHS to produce a well-distributed set of input samples, e.g., $N = 1000$. A key innovation of the proposed framework is that it avoids using the entire pool for every output. Since the complexity of the LF response may vary significantly across outputs, the number of samples required to characterize each response also differs significantly. To address this, a preliminary adaptive sizing procedure is introduced to determine an optimal, output-specific subset of candidates. Before entering the main AL loop, the LF data of each output j are analyzed to find the minimum number of samples $N_{\text{LF},j}$ required for the mean and standard deviation of the LF response to stabilize. This process yields a set of tailored candidate pools, $\mathcal{U}_j \subset \mathcal{U}_{\text{master}}$, each adaptively sized to match the complexity of the corresponding response. Specifically, let $\mu_{j,n}$ and $\sigma_{j,n}$ denote the LF sample mean and standard deviation computed on the first n samples for output j. The smallest n satisfying, for r consecutive increments of Δn,

$$\frac{|\mu_{j,n} - \mu_{j,n-\Delta n}|}{|\mu_{j,n-\Delta n}| + \varepsilon} \le \epsilon_\mu, \qquad \frac{|\sigma_{j,n} - \sigma_{j,n-\Delta n}|}{\sigma_{j,n-\Delta n} + \varepsilon} \le \epsilon_\sigma, \tag{24}$$

is taken as $N_{\mathrm{LF},j}$ and defines the specific pool $\mathcal{U}_j$. In Eq. (24), the stability tolerances are taken equal, and values in the range $\epsilon_\mu = \epsilon_\sigma \in [0.01,\ 0.03]$ lead to essentially identical LF pool sizes.

The following AL iterations for each model are restricted to their respective pools, avoiding redundant variance evaluations and improving overall computational efficiency. Importantly, all HF evaluations are drawn from within the LF pool, yielding a strictly nested experimental design, $\mathcal{D}_H \subset \mathcal{D}_L$, as recommended by Toal [86]. This guarantees that every HF point has a collocated LF prediction.

The core principle of AL is to iteratively refine the surrogate model by querying the HF simulation at the most informative locations. This process is guided by an acquisition function, which scores each candidate point $\mathbf{x}^*$ based on its potential to improve the model. In this study, we employ an uncertainty sampling strategy, adopting the GPR's posterior predictive variance as the acquisition function [67,87,88]:

$$s^2_\Delta(\mathbf{x},\zeta_p) = k_\theta\big((\mathbf{x},\zeta_p),(\mathbf{x},\zeta_p)\big) - \mathbf{k}^{\mathsf{T}}_{\mathbf{x},p}\,\mathbf{K}^{-1}\mathbf{k}_{\mathbf{x},p}, \qquad \mathbf{k}_{\mathbf{x},p} = K_\theta\big((\mathbf{x},\zeta_p),\tilde{\mathbf{X}}\big) \in \mathbb{R}^N. \tag{25}$$

where $s^2_\Delta(\mathbf{x},\zeta_p)$ is the posterior variance of the discrepancy $\delta_g(\mathbf{x},\zeta_p)$ at the candidate location $(\mathbf{x},\zeta_p)$, computed on the current HF training set $(\tilde{\mathbf{X}},\mathbf{y}_w)$. Here, $\mathbf{K}$ is the covariance matrix of the HF training data, $\mathbf{k}_{\mathbf{x},p}$ the covariance vector between the candidate and the training points, and σ_n^2 the regularization term that stabilizes the inversion of $\mathbf{K}$.

To compute a comprehensive uncertainty measure for each input candidate, the pointwise variances along the thickness are aggregated into an acquisition score for each output j:

$$S_j(\mathbf{x}) = \sum_{p=1}^{P} w_{j,p}\, s^2_\Delta(\mathbf{x},\zeta_p). \tag{26}$$

Here, j denotes the output type (e.g., a specific stress component or failure index), and $p = 1,\dots,P$ refers to a discrete node along the thickness. The weights $w_{j,p} > 0$ satisfy $\sum_{p=1}^{P} w_{j,p} = 1$. When uniform weights are used ($w_{j,p} = 1/P$), $S_j(\mathbf{x})$ represents the average epistemic uncertainty through the thickness. Alternatively, non-uniform weighting profiles can be defined to emphasize regions where higher accuracy is required. Finally, Eq. (27) is used to select the next HF evaluation for output j by maximising the aggregated score across its candidate pool U_j. This targets the location where the epistemic uncertainty of the discrepancy is greatest.

$$\mathbf{x}_j^{\mathrm{next}} \in \arg\max_{\mathbf{x}\in\mathcal{U}_j} S_j(\mathbf{x}). \tag{27}$$

As the various structural responses differ in complexity, the proposed AL framework handles each output independently, while maintaining consistency across all quantities. This is summarised in Algorithm 1 and involves three distinct phases at each iteration.

1. **Identification of Informative Candidates.** Each active (i.e., non-converged) output independently selects a small subset of input points from a shared sampling space. These candidates correspond to regions of high epistemic uncertainty, as quantified by the GPR predictive variance.
2. **Construction of a Global Candidate Set.** The individual proposals are aggregated into a global candidate set for the current iteration. This step ensures that the distinct uncertainty profiles of all active models are considered together prior to final point selection.
3. **Final Selection.** A final batch of points is selected from the global set for HF evaluation. When multiple candidate points are available, selection is guided by aggregate informativeness, prioritizing points with the highest average predictive variance while maintaining diversity across all models. To this end, each candidate $\mathbf{x}$ is scored through a penalized acquisition function [89,90]:

$$\Phi_j(\mathbf{x};\mathcal{B}) = S_j(\mathbf{x}) \prod_{\mathbf{u}\in\mathcal{B}} \Big(1 - \exp\big\{-\tfrac{\|\mathbf{x}-\mathbf{u}\|^2}{2\lambda^2_{\mathrm{div}}}\big\}\Big), \tag{28}$$

Here, $S_j(\mathbf{x})$ is the cumulative variance score, $\mathcal{B}$ is the set of already selected points in the current batch, and λ_{div} controls the diversification penalty typically set to the median pairwise distance among candidates. The exponential term in Eq. (28) lowers the score of candidates located too close to previously selected points, promoting spatial diversity and avoiding redundant evaluations. Batch construction proceeds over the candidate pool $\mathcal{U}_j$ until the target batch size $|\mathcal{B}| = B$ is reached.

The learning process for each output is governed by a specific set of stopping criteria, which are described in Section 3.3

3.3. Monte Carlo verification

In order to verify that the MF surrogate reproduces not only the available HF data but also the full probabilistic behaviour over the input domain, verification is performed against a HF Monte Carlo (MC) baseline. Two HF references are considered (see Section 4.2): (i) a CUF LW model as explained in Section 2 and (ii) a 3D FE model in Abaqus (C3D8R). For consistency, both the MC-HF simulations and the MF surrogate predictions are evaluated on the same validation set $\mathcal{X}_{\mathrm{val}} = \{\mathbf{x}^{(i)}\}_{i=1}^{N_{\mathrm{val}}}$ and at the same thickness nodes $\{\zeta_p\}_{p=1}^{P}$, so that every metric is computed on identical inputs and spatial locations.

For each response $y(\mathbf{x},\zeta)$, the quantity is evaluated at a discrete set of normalized thickness coordinates $\{\zeta_p\}_{p=1}^{P}$, thus providing its complete through-thickness profile. Two quantities are analyzed: the full profile itself and the corresponding maximum value along the thickness,

$$y^{\max}(\mathbf{x}) = \max_{\zeta\in[-1,1]} y(\mathbf{x},\zeta), \tag{29}$$

Algorithm 1 Multi-fidelity multi-output framework with adaptive selection.

Initialize training sets $\mathcal{D}_L$ (LF), $\mathcal{D}_H$ (HF) ▷ Initial DoE
Generate a master candidate pool $\mathcal{U}_{\text{master}}$ by LHS; standardize inputs
— Phase 0: Preliminary LF adaptive sizing —
for all output $j = 1, \dots, N_{\text{outputs}}$ **do** ▷ For each output
  Determine $N_{\text{LF},j}$ via stabilization (Eq. (24))
  Define $\mathcal{U}_j \subset \mathcal{U}_{\text{master}}$ with $|\mathcal{U}_j| = N_{\text{LF},j}$
end for
— Phases 1–3: iterative active learning —
while stopping criteria not met **and** budget not exceeded **do**
  $\mathcal{C}_{\text{next}} \leftarrow \emptyset$
  for all active output j **do**
    Train/update MF-GPR M_j on $\mathcal{D}_H$ (discrepancy in $g(\cdot)$; using separable kernel)
    For all $\mathbf{x} \in \mathcal{U}_j$: compute $s^2_\Delta(\mathbf{x}, \zeta_p)$ (Eq. (25))
    Aggregate $S_j(\mathbf{x})$ over ζ_p (Eq. (26))
    $\mathcal{C}_j \leftarrow \arg\max^k_{\mathbf{x}\in\mathcal{U}_j} S_j(\mathbf{x})$ ▷ Top-k proposals
    $\mathcal{C}_{\text{next}} \leftarrow \mathcal{C}_{\text{next}} \cup \mathcal{C}_j$
  end for
  Remove duplicates from $\mathcal{C}_{\text{next}}$; let $\mathcal{J}_{\text{act}}$ be the set of active outputs
  Batch selection (size B): set $\mathcal{B} \leftarrow \emptyset$
  while $|\mathcal{B}| < B$ **do**
    For all $\mathbf{x} \in \mathcal{C}_{\text{next}} \setminus \mathcal{B}$ and $j \in \mathcal{J}_{\text{act}}$, evaluate $\Phi_j(\mathbf{x}; \mathcal{B})$ *as in* Eq. (28)
    $\overline{\Phi}(\mathbf{x}) \leftarrow |\mathcal{J}_{\text{act}}|^{-1} \sum_{j\in\mathcal{J}_{\text{act}}} \Phi_j(\mathbf{x}; \mathcal{B})$
    $\mathbf{x}^\star \leftarrow \arg\max_{\mathbf{x}} \overline{\Phi}(\mathbf{x})$; $\mathcal{B} \leftarrow \mathcal{B} \cup \{\mathbf{x}^\star\}$
  end while
  Run HF at all $\mathbf{x} \in \mathcal{B}$;
  $\mathcal{D}_H \leftarrow \mathcal{D}_H \cup \{(\mathbf{x}, f_H(\mathbf{x})) : \mathbf{x} \in \mathcal{B}\}$ ▷ Update training set $(\mathbf{x}, f_H(\mathbf{x}))$ to $\mathcal{D}_H$
  For all j: $\mathcal{U}_j \leftarrow \mathcal{U}_j \setminus \mathcal{B}$; check stopping criteria for M_j
end while

which is relevant when the assessment focuses on peak responses, such as layerwise stresses or failure indices.

The MC–HF reference is generated progressively in batches of size N_{batch}. After each batch n, the sample mean μ_n and standard deviation σ_n of the accumulated maxima $\{y^{\max}(\mathbf{x}^{(i)})\}_{i=1}^{nN_{\text{batch}}}$ are updated. Convergence is assessed by monitoring the relative variation of these statistics between r consecutive batches:

$$\frac{|\mu_n - \mu_{n-1}|}{|\mu_{n-1}| + \varepsilon} \le \epsilon_\mu, \qquad \frac{|\sigma_n - \sigma_{n-1}|}{\sigma_{n-1} + \varepsilon} \le \epsilon_\sigma, \tag{30}$$

The parameters ϵ_μ and ϵ_σ define the target accuracy and are set to 0.01. In this way, the MF-GPR and MC-HF baselines are compared under identical conditions: (i) using the same validation inputs $\mathcal{X}_{\text{val}}$ and thickness nodes ζ_p; (ii) applying equivalent accuracy-based stopping rules, which are applied to the same distributional functionals (through-thickness mean and standard-deviation profiles, and the distribution of maxima $y^{\max}$). The MF-GPR model terminates once the mean predictive accuracy reaches $R^2 \ge 0.95$, and the epistemic uncertainty, quantified as the 95% confidence-band width, drops below 1% of the data range. After termination of both procedures, comparability is verified a posteriori on the same statistics: the relative deviations between MF-GPR and MC-HF through-thickness mean and standard-deviation profiles remain within the same tolerance thresholds $(\epsilon_\mu, \epsilon_\sigma)$ used in Eq. (30), and the discrepancy between the probability density of $y^{\max}$ is negligible. This ensures that both methods are evaluated at a comparable and statistically consistent level of accuracy. The complete probabilistic framework is schematically summarized in Fig. 3. The diagram illustrates the interplay between the MF surrogate model, the iterative AL loop that guides its training, and the final MC validation stage that assesses its predictive accuracy.

4. Numerical results

4.1. Non probabilistic failure prediction under material and load uncertainties

This section presents numerical results that demonstrate the predictive capabilities of the MF surrogate model based on the additive correction strategy introduced in Section 3.1. The test case is a twelve-layer symmetric $[30°/0°]_{4S}$ laminate ($a = b = 0.5$ m, $h = 1.5$ mm) subjected to the boundary and loading conditions shown in Fig. 4. Uncertainties are introduced via two independent, identically distributed Gaussian factors: $\xi_{\text{mat}} \sim \mathcal{N}(0, 0.1^2)$ perturbs the material's elastic and strength properties (Table 1). For instance, a generic material property P is updated from its nominal value P_{nom} according to the relation:

$$P_{\text{rand}} = P_{\text{nom}} \cdot (1 + \xi_{\text{mat}}) \tag{31}$$

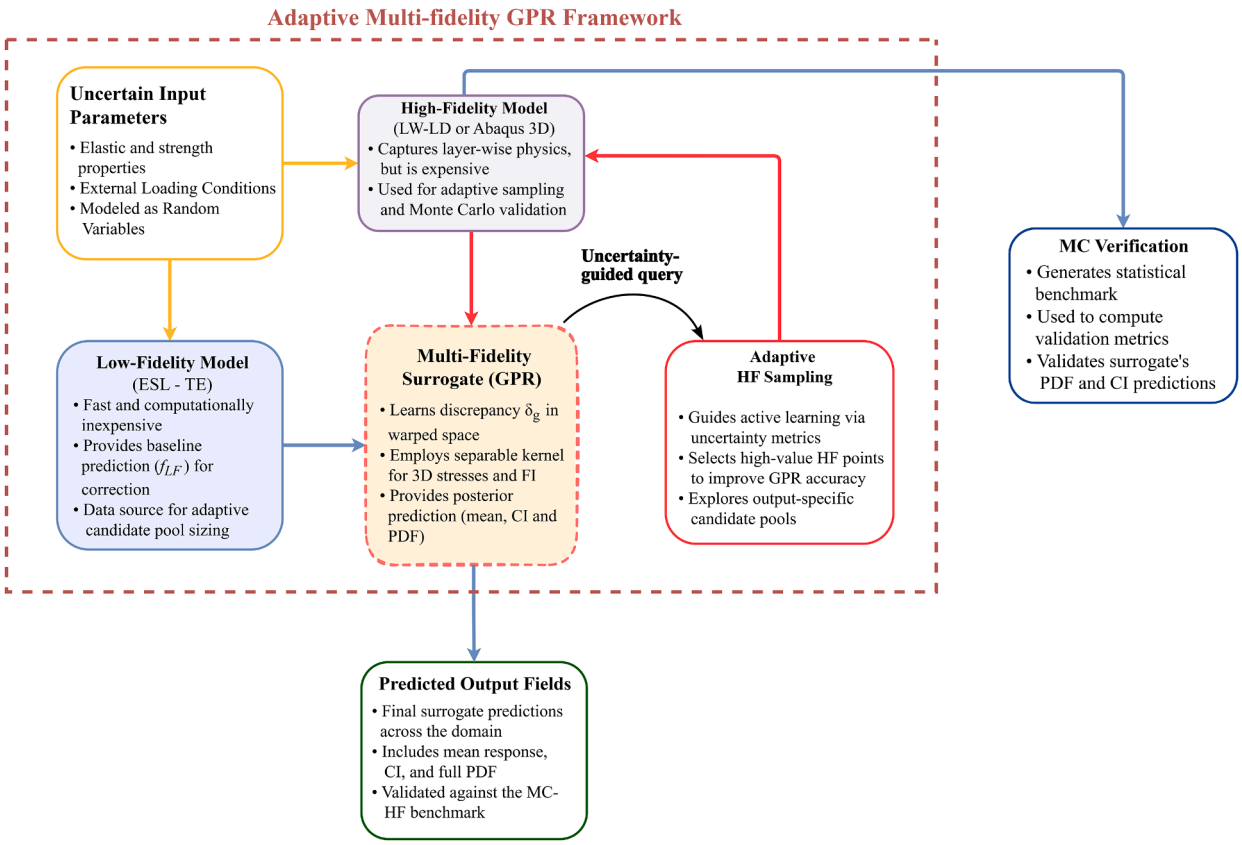

Fig. 3. Flow-chart of the integrated MF framework for uncertainty quantification, detailing the AL training cycle and validation.

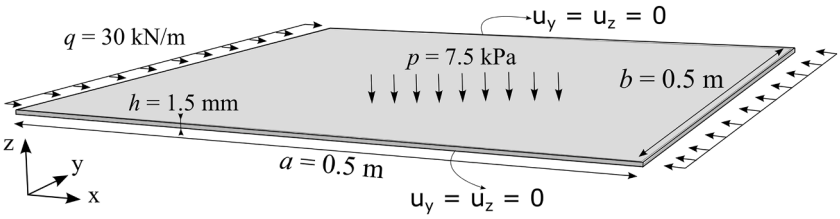

Fig. 4. Boundary conditions and loading of the laminated plate.

Table 1
Nominal elastic and strength properties of the laminate.

Elastic property	Value	Strength property	Value
E_1 [GPa]	143.0	X_T [MPa]	1690
E_2, E_3 [GPa]	9.1	X_C [MPa]	800
G_{12}, G_{13} [GPa]	4.8	Y_T [MPa]	28
G_{23} [GPa]	4.8	Y_C [MPa]	100
ν_{12}, ν_{13}	0.30	S_{12} [MPa]	75
ν_{23}	0.30	$S_{23} = S_{13}$ [MPa]	75

A second, independent factor $\xi_{\text{load}} \sim \mathcal{N}(0, 0.1^2)$ perturbs the transverse line load q and surface pressure p. This case employs two distinct levels of fidelity, both on a 10×10 Q9 mesh: LF responses are generated by an ESL model with TE1 expansion through-the-thickness (ESL-TE1), while HF responses are obtained from a more refined LW model utilizing a 2 LD3 expansion function for each layer. The MF surrogate is subsequently trained on a small, strictly nested DoE of ten points, comprising 70% LF runs and 30% HF runs ($\mathcal{D}_{\text{HF}} \subset \mathcal{D}_{\text{LF}}$), as detailed in Section 3.2.

Fig. 5 first compares the LF, HF, and MF predictions for the maximum through-thickness values of the Hashin 3D failure indices (see Appendix A) as a function of the material factor ξ_{mat} alone. Fig. 6 then extends the analysis to the two-parameter space ($\xi_{\text{mat}}, \xi_{\text{load}}$),

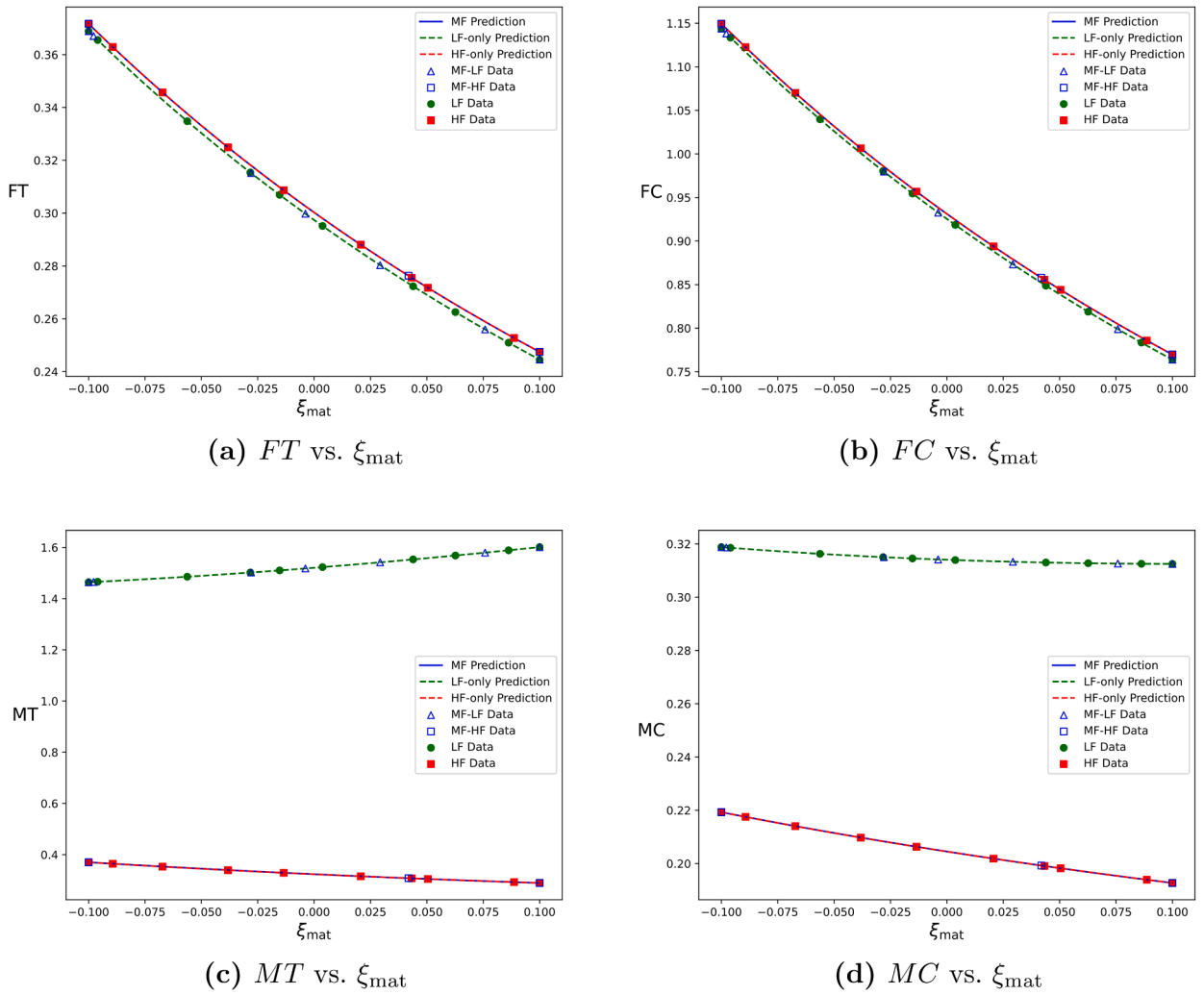

Fig. 5. Predictions of FI under material uncertainty (ξ_{mat}), comparing LF-only, HF-only, and MF-GPR models. Markers denote the training samples: MF-LF Data and MF-HF Data are the LF/HF sets used by the proposed MF-GPR strategy (LF pool and adaptively selected HF points), whereas LF Data and HF Data correspond to the training sets used to build the LF-only and HF-only response baselines, respectively.

showing the MF response surfaces together with the scattered LF and HF training samples. Based on these results, the following key observations can be made:

- For the fiber-dominated indices (FT, FC), the LF model provides a sufficiently accurate baseline, with predictions closely matching the HF results in both the 1D and 2D uncertainty space. The MF surrogate perfectly aligns with the HF only model.
- For the matrix-dominated indices (MT, MC), the LF model proves inadequate. Notably, it fails to capture complex transverse shear effects, leading to a significant overprediction of the MT index and an erroneous failure prediction (FI > 1). This highlights a critical risk in design optimization, where such a model would lead to the false rejection of a valid design. In contrast, the MF surrogate successfully corrects this physical inaccuracy and reproduces the high-fidelity behavior with high precision. This capability is maintained in the more complex 2D uncertainty space.
- The HF model, based on a refined LW kinematic, predicts values well below the failure onset. In contrast, the LF model, derived from a simplified theory similar to FSDT, significantly overestimates the MT and MC indices due to its limited capability to represent shear effects. The MF model, trained with only 30% of the HF simulations, effectively compensates for this limitation and reproduces the HF predictions.

4.2. Probabilistic stress and failure analysis of a composite plate

This section demonstrates the capability of the adaptive MF-GPR framework (Section 3.2) to achieve efficient and accurate uncertainty propagation in multilayered composites. The benchmark problem [91] consists of a two-layer cross-ply laminate with stacking

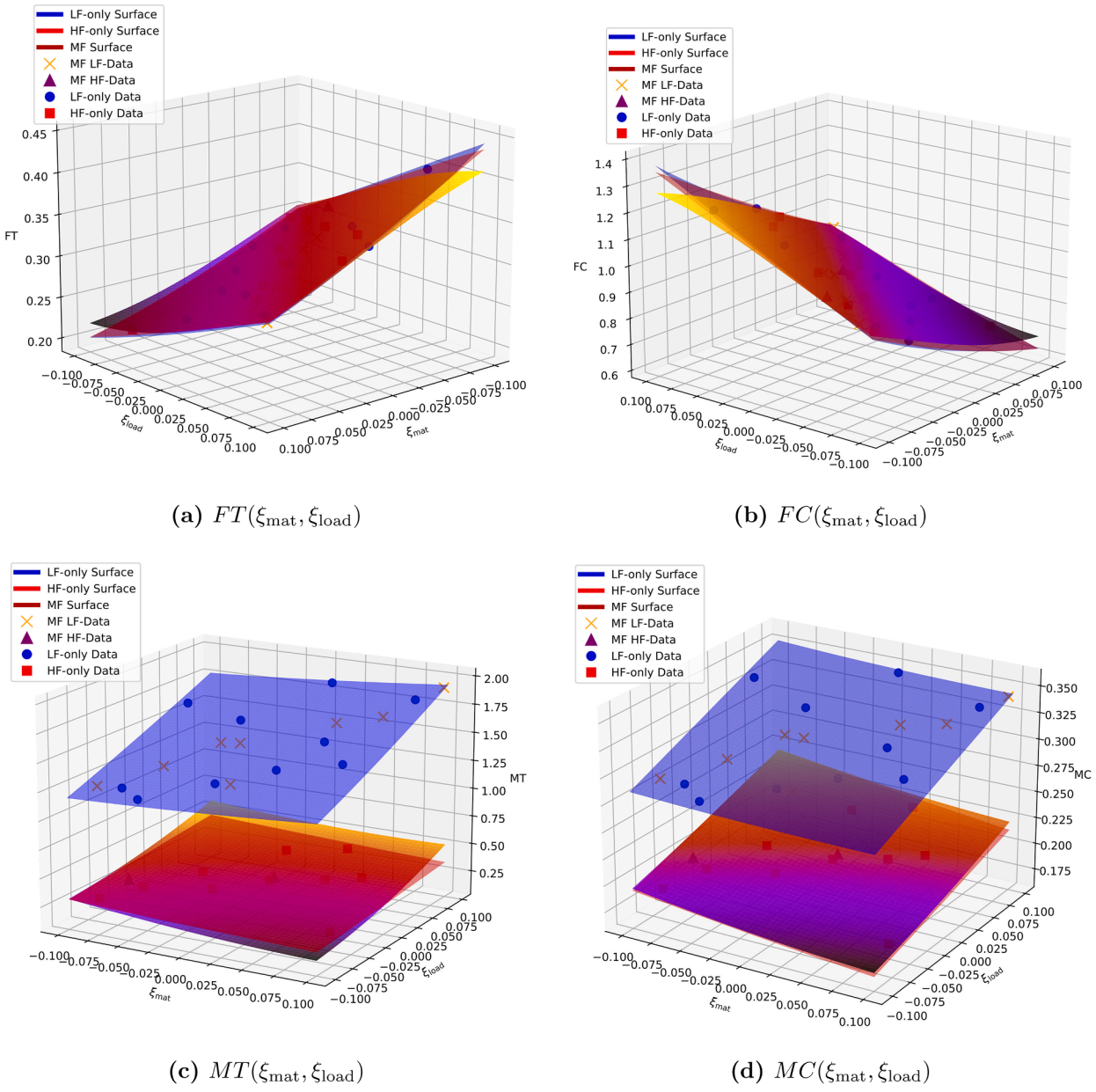

(a) $FT(\xi_{\text{mat}}, \xi_{\text{load}})$ (b) $FC(\xi_{\text{mat}}, \xi_{\text{load}})$

(c) $MT(\xi_{\text{mat}}, \xi_{\text{load}})$ (d) $MC(\xi_{\text{mat}}, \xi_{\text{load}})$

Fig. 6. Predictions of FI under material (ξ_{mat}) and load (ξ_{load}) uncertainties, comparing LF-only, HF-only, and MF-GPR models. Markers indicate the training samples: MF-LF Data and MF-HF Data are the LF/HF sets used by the proposed MF-GPR strategy, whereas LF Data and HF Data correspond to the training sets used to build the LF-only and HF-only baselines, respectively.

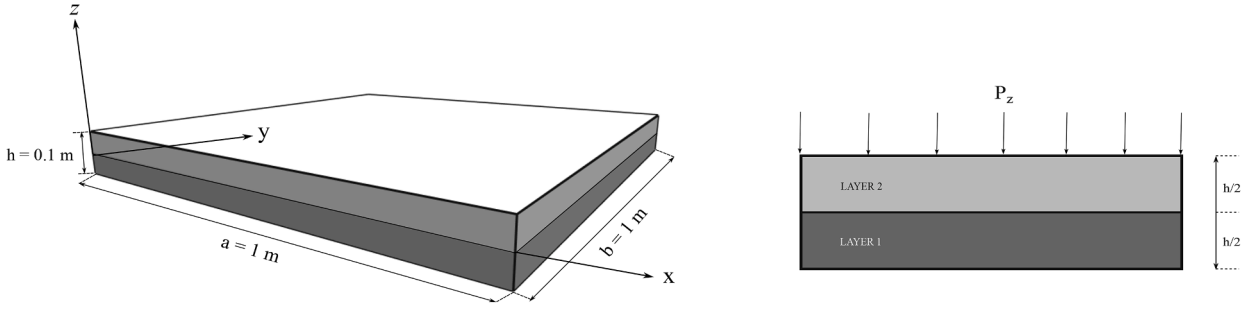

Fig. 7. Boundary conditions and loading of the laminate plate.

Table 2
Statistical description of material properties and load.

Elastic properties			Strengths & load		
Parameter	Mean	CoV [%]	Parameter	Mean	CoV [%]
E_1 [GPa]	137.9	5.0	P_z [kPa]	10	10.0
E_2 [GPa]	8.96	13.5	X_T [MPa]	2500	5.0
E_3 [GPa]	8.96	13.5	X_C [MPa]	1600	5.0
G_{12} [GPa]	7.10	14.5	Y_T [MPa]	90	11.0
G_{13} [GPa]	7.10	14.5	Y_C [MPa]	300	13.5
G_{23} [GPa]	6.21	14.5	S_{12} [MPa]	120	16.5
ν_{12} [–]	0.30–0.33	–	S_{23} [MPa]	120	16.5
ν_{13} [–]	0.30–0.33	–	Z_T [MPa]	60	13.5
ν_{23} [–]	0.49–0.55	–			

sequence [90°/0°], in-plane dimensions $a = b = 1$ m, and thickness $h = 0.1$ m, subjected to a uniform transverse pressure P_z (see Fig. 7). Table 2 summarizes the statistical characterization of the material and load parameters. The mean values correspond to the nominal mechanical properties, while the Coefficients of Variation (CoV) quantify their relative uncertainty. Variability is introduced in both the elastic and strength properties of the composite, as well as in the applied load. The elastic constants are modeled as Gaussian random variables with CoV values ranging from 5% to 15% [92–95], capturing the lower variability of fiber-dominated directions and the higher dispersion of matrix-dominated ones. Strength parameters are also assumed normally distributed, with CoV values between 5% and 20% [96–98], depending on the corresponding failure mode. Poisson's ratios are represented through uniform distributions within admissible bounds [99], whereas the applied pressure P_z is perturbed by a 10% CoV to account for load uncertainty [100]. As in the previous case, two levels of fidelity are employed, both based on a 10×10 Q9 FE mesh in the plate plane, whose size was selected after a convergence study. LF responses are generated by an ESL model with TE1 expansion through-the-thickness (ESL-TE1, 2646 DOF), whereas HF responses are obtained from a refined LW model utilizing a 2 LD3 expansion function for each layer (17199 DOF) and a 3D Abaqus model employing a $80 \times 80 \times 16$ solid C3D8R elements ($\approx$ 300000 DOF), as used in Ref. [91].
Table 3 summarizes the quantitative comparison between the MF-GPR surrogate and the MC-HF reference. For each output, the table lists the number of low- and high-fidelity simulations (N_{LF}, N_{HF}), the percentage of HF data used (%HF), and the statistical indicators of predictive accuracy: the coefficient of determination (R^2) and the normalized root mean square error (nRMSE) repored in Eq. (32). The last column reports the number of HF MC samples used as reference; it is the minimum size meeting the stopping criteria in Eq. (30), which guarantees that the HF benchmark and the MF model evaluated at equivalent levels of accuracy (see Section 3.3). As a complement to Table 3, the minimum and maximum through-thickness errors are listed. The in-plane stresses show the following ranges: σ_{xx} between 0.04% and 1.44%, σ_{yy} between 0.04% and 1.30%, and σ_{xy} between 0.04% and 0.85%. For out-of-plane responses, the transverse normal stress σ_{zz} lies between 0.23% and 1.45%, while the shear components remain contained, with σ_{xz} within 0.11% to 0.81% and σ_{yz} within 0.12% to 0.98%. Regarding the failure indices, FT ranges from 0.09% to 1.64%, FC from 0.02% to 0.83%, MT from 0.18% to 1.41%, and MC from 0.03% to 1.34%; the delamination index ranges from 0.13% to 0.93%.

$$R^2 = 1 - \frac{\sum_i (y_i^{\mathrm{MF}} - y_i^{\mathrm{HF}})^2}{\sum_i (y_i^{\mathrm{HF}} - \bar{y}^{\mathrm{HF}})^2}, \qquad \mathrm{nRMSE} = \frac{\sqrt{\frac{1}{N}\sum_i (y_i^{\mathrm{MF}} - y_i^{\mathrm{HF}})^2}}{\max(y^{\mathrm{HF}}) - \min(y^{\mathrm{HF}})}. \tag{32}$$

In addition to the accuracy indicators in Eq. (32), performance is also quantified under an equal computational budget by comparing the proposed MF-GPR strategy against MC-HF using the measured LF/HF cost ratio. To quantify the discrepancy, two additional error measures are introduced in the uncertainty propagation along the thickness coordinate z:

$$E_{\mathrm{CI}} = \frac{\left\langle \left| Q_{0.95}(z) - q_{0.95}^{\mathrm{ref}}(z) \right| \right\rangle_z + \left\langle \left| Q_{0.05}(z) - q_{0.05}^{\mathrm{ref}}(z) \right| \right\rangle_z}{\Delta y_{\mathrm{ref}}}, \qquad E_\sigma = \frac{\left\langle \left| \sigma(z) - \sigma^{\mathrm{ref}}(z) \right| \right\rangle_z}{\left\langle \sigma^{\mathrm{ref}}(z) \right\rangle_z}. \tag{33}$$

Here, E_{CI} quantifies the discrepancy between the predicted and reference 90% confidence bounds, while E_σ evaluates the accuracy of the estimated standard deviation along the laminate thickness. In these expressions, $(\cdot)^{\mathrm{ref}}$ denotes the converged HF benchmark (see Table 3); $\langle \cdot \rangle_z$ represents the spatial average across the thickness; and $\Delta y_{\mathrm{ref}} = \max(y^{\mathrm{ref}}) - \min(y^{\mathrm{ref}})$ is used as the normalization factor. To compare MF-GPR against MC-HF under the same computational budget, Table 3 reports the equal-cost confidence-envelope factor $F_{\mathrm{CI}} = E_{\mathrm{CI}}^{\mathrm{HF,eq}} / E_{\mathrm{CI}}^{\mathrm{MF}}$. The companion factor $F_\sigma = E_\sigma^{\mathrm{HF,eq}} / E_\sigma^{\mathrm{MF}}$, which evaluates the agreement of the standard-deviation profile $\sigma(z)$ along the thickness, is discussed here for completeness. For instance, at an equal computational cost, MF-GPR improves the confidence envelope accuracy by approximately +68% for σ_{yy}, +120% for σ_{xy}, +56% for σ_{xz}, and +90% for σ_{zz}. Correspondingly, the prediction of through-thickness variability is enhanced by roughly +77%, +105%, +80%, and +67% for the respective components. A similar trend is observed for failure-related quantities (see Table 3). For instance, the confidence-envelope error is reduced by about +69% for FT and +62% for the delamination index, with corresponding improvements of roughly +110% and +60% in the variability profile. For each output j reported in Table 3, the LF dataset is the output-specific candidate pool U_j whose size $N_{LF,j}$ is determined by the criterion introduced in Section 3.2 (Eq. (24)), and therefore it can vary among outputs. The MF model is initialized with a small nested set of co-located HF samples $D_{H,0} \subset U_j$, while the remaining HF evaluations reported in Table 3 are added iteratively by the adaptive learning loop by selecting new analyses that maximize the aggregated acquisition function, consistently with Section 3.2

Table 3
Multi-fidelity performance metrics for stresses and failure indices, evaluated along the thickness at the in-plane point $(-a/4, -b/4)$, with reference to the MC–HF benchmark. The factor F_{CI} evaluates the accuracy of the confidence intervals at equal computational cost.

Output	N_{LF}	N_{HF}	%HF	R^2	nRMSE	F_{CI}	MC-HF
Stresses							
σ_{xx}	200	80	40.0%	0.995	0.010	1.45	600
σ_{yy}	300	65	21.7%	0.998	0.009	1.68	600
σ_{zz}	195	150	76.9%	0.999	0.006	1.90	600
σ_{xz}	200	163	81.5%	1.000	0.005	1.56	600
σ_{yz}	250	175	70.0%	1.000	0.004	1.57	600
σ_{xy}	300	20	6.7%	1.000	0.005	2.20	600
Failure indices							
FT	300	70	23.3%	0.992	0.010	1.69	600
FC	150	49	32.7%	0.999	0.006	1.29	600
MT	150	65	43.3%	0.997	0.008	1.80	600
MC	450	65	14.4%	0.998	0.007	2.11	600
delam	400	300	75.0%	0.999	0.007	1.62	600

Table 4
Total computational time and speedup of the MF framework compared to HF benchmarks. S_{CUF} and S_{ABQ} indicate the speedup of the GPR-MF framework with respect to the MC-HF performed with CUF and Abaqus 3D, respectively.

Output	T_{MF} [min]	S_{CUF}	S_{ABQ}
Stresses			
σ_{xx}	11.5	3.99	6.36
σ_{yy}	13.0	3.52	5.61
σ_{zz}	16.7	2.75	4.38
σ_{xz}	17.8	2.57	4.10
σ_{yz}	20.1	2.28	3.64
σ_{xy}	9.6	4.78	7.62
Failure indices			
FT	13.4	3.42	5.45
FC	7.8	5.90	9.40
MT	9.0	5.10	8.12
MC	17.0	2.69	4.28
delam	33.6	1.36	2.17

(Eqs. (28) to (28)). This sampling procedure is illustrated in Appendix B (see Fig. B.17), which reports the adaptive-learning HF sample allocation for the delamination index, the most demanding output listed in Table 3, as a projection onto the input uncertainty plane (S_{13}, S_{23}), i.e., the shear strength parameters with the strongest influence on the delamination index. Furthermore, Appendix B provides a direct comparison between adaptive and non-adaptive MF-GPR schemes at an equal computational cost. The analysis demonstrates that a static HF design fails to capture the confidence bands for the out-of-plane and shear stress components (σ_{zz}, σ_{xz}, and σ_{yz}) and the delamination index, whereas the adaptive framework successfully reconstructs an accurate uncertainty envelope for these quantities. Table 4 reports the overall computational cost of the multi-fidelity framework. The total runtime was evaluated as the cumulative contribution of the low- and high-fidelity CUF simulations required for each output, with average execution times of $t_{LF} = 1.61$ s and $t_{HF} = 4.58$ s, respectively. For comparison, the corresponding Abaqus 3D simulation required $t_{ABQ} = 7.30$ s. The last two columns show the corresponding speedup factors with respect to MC using CUF-based HF or 3D Abaqus models. These values quantify the computational efficiency gain achieved by the MF-GPR framework. All simulations were performed on an Intel(R) Core(TM) Ultra 7 155H CPU @ 1.40 GHz.

Figs. 8 and 9 present the through-the-thickness distributions of stresses and failure indices evaluated at the point $(-a/4, -b/4)$, as referenced in Ref. [91]. For each output, two comparisons are reported: (a) the MC simulations using CUF-based high-fidelity models (MC–HF) versus the MF-GPR surrogate (see Section 3.2), displaying the mean response and the 90% confidence interval under the uncertainties reported in Table 2; and (b) an MC benchmark using the 3D Abaqus model as reference, also showing the mean and the corresponding 90% confidence interval under the same uncertainty conditions. For the sake of completeness, the corresponding results for the non-adaptive MF-GPR surrogate can be found in Appendix B. Fig. 10 shows a comparison of the Probability Density Functions (PDF) of the maximum failure indices across the thickness under the considered uncertainties. The MC-HF results are compared with the MF-GPR surrogate for the FT, MC and Delamination indices.
From the results shown, the following comments can be drawn:

Table 5
Statistical description of material properties and load.

Elastic properties			Strengths & load		
Parameter	Mean	CoV [%]	Parameter	Mean	CoV [%]
E_1 [GPa]	137.9	5.0	ϵ_{yy} [–]	0.01	10.0
E_2 [GPa]	14.5	8.5	X_T [MPa]	2500	5.0
E_3 [GPa]	14.5	8.5	X_C [MPa]	1600	5.0
G_{12} [GPa]	5.9	16.5	Y_T [MPa]	90	11.0
G_{13} [GPa]	5.9	16.5	Y_C [MPa]	300	13.5
G_{23} [GPa]	5.9	16.5	S_{12} [MPa]	120	16.5
ν_{12} [–]	0.21–0.25	–	S_{23} [MPa]	120	16.5
ν_{13} [–]	0.21–0.25	–	Z_T [MPa]	60	13.5
ν_{23} [–]	0.21–0.25	–			

- For the in-plane stresses (σ_{xx}, σ_{yy}, σ_{xy}), only a minimal discrepancy is observed between the HF and LF models (see Fig. 8a). Both the adaptive and non-adaptive MF-GPR surrogates (see also Fig. B.18a in Appendix B) reproduce the HF benchmarks both CUF-based and 3D Abaqus (see Fig. 8b), showing no significant deviation in either the mean profiles or the confidence intervals.
- For the out-of-plane stresses (σ_{xz}, σ_{yz}, σ_{zz}), a substantial discrepancy emerges between LF and HF (see Fig. 8c and e). The non-adaptive GPR–MF (Fig. B.18b and c) fails to reproduce the HF confidence bands at the laminate top and bottom because the underlying classical ESL-TE1 (similar to FSDT) typically overlook the C_z^0 requirements and do not satisfy equilibrium conditions pointwise, especially at the at the top and bottom edges of the plate. In contrast, the adaptive GPR-MF matches both HF mean profiles and confidence intervals (Fig. 8d and f) by directing HF samples to the high-variance zones, thus effectively learning the non-linear correction to apply to the LF model.
- For the failure indices, two different behaviors can be observed. For the fiber- and matrix-dominated modes (FT, FC, MT, MC), the discrepancy between LF and HF is limited (see Figs. 9a, 9c, 9e, 9g), which makes it relatively easy to learn the correction profile and build an accurate MF surrogate. For the delamination index, instead, the LF model completely fails to reproduce the through-thickness profile as seen in Fig. 9c, since this quantity depends solely on out-of-plane stresses (see Appendix A). As a consequence, the non-adaptive GPR–MF (Fig. B.18h) cannot capture either the mean trend or the confidence intervals, and only the adaptive surrogate provides a reliable prediction consistent with the HF benchmarks (Fig. 9d).
- Fig. 10 shows the comparison between MF-GPR and MC-HF PDF of the maximum failure indices. The MF-GPR surrogate accurately reproduces the CUF HF reference, with minor deviations observed in the tails, particularly for the delamination index, which remains the most demanding case due to the stronger nonlinear correction function and higher sensitivity to uncertainties.

4.3. Probabilistic free-edge stresses

This case study shows the capability of the proposed MF framework to reproduce free-edge effects induced by the mismatch of orthotropic properties at ply interfaces in the presence of uncertainties. The benchmark laminate presented in [101] is considered. The beam has a stacking sequence $[45°/-45°]_s$, with each layer of equal thickness, and is subjected to a uniform longitudinal strain $\epsilon_{yy} = 0.01$ at the ends. Geometry and loading are shown in Fig. 11. Similarly to the previous section, Table 5 summarizes the statistical characterization of the material and load parameters, where the mean values correspond to the nominal properties and the CoV quantify their uncertainty. The elastic moduli, strength allowables, and applied load follow normal distributions, whereas the Poisson ratios are modeled as uniform random variables. In this case, the LF analyses are generated by an ESL model with TE2 expansion through-the-thickness (ESL-TE2, 3969 DOF), while HF results are obtained through a LW model with 2 LD3 for each ply (33075 DOF).

The results focus on the transverse shear stress σ_{yz}, which develops near the free edge, specifically the evolution at mid-span ($y = L/2$) and $z/h = 0.25$, starting from the free edge ($x/b = 0.5$) and moving toward the plate center; as well as its variation through the thickness at the same span-wise coordinate along the free-edge section. Table 6 summarizes the corresponding performance and computational metrics, including the number of low- and high-fidelity samples, accuracy with respect to the CUF-based MC–HF benchmark, the equal-cost confidence-envelope factor F_{CI}, and the achieved computational speedup. The average runtimes of the CUF low- and high-fidelity models are $t_{\mathrm{LF}} = 2.27$ s and $t_{\mathrm{HF}} = 6.75$ s, respectively. Figs. 12 and 13 illustrate the probabilistic transverse shear stress σ_{yz} obtained along the two free-edge paths described. For each output, (a) reports the mean value and 90% confidence intervals obtained from the CUF-based HF, and also the mean values obtained with LF and MF (see Figs. 12a and 13a), and b) shows the corresponding adaptive MF-GPR predictions, which provide the mean response and 90% confidence interval under the same uncertainty conditions defined in Table 6 (see Figs. 12b and 13b).

From the results outlined, the following comments can be made:

- Fig. 12 shows that the MF surrogate accurately captures the stress gradients σ_{yz} near the free edge, reproducing both the HF mean trends and the 90% confidence bands along x-direction due to uncertainties. Similarly, Fig. 13 illustrates that the MF model presents the correct through-thickness mean value and confidence intervals, while the LF model is not able to capture the interlaminar stress profile accurately.

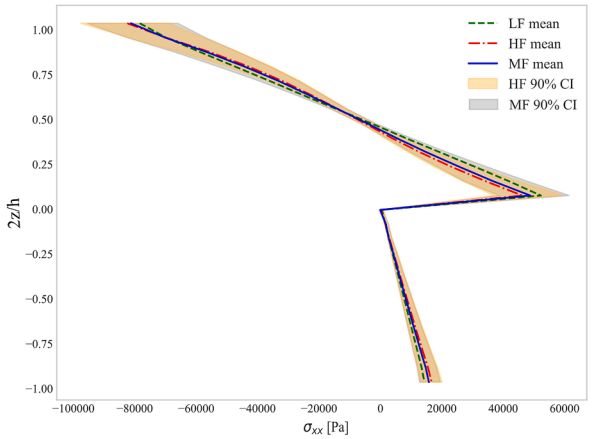

(a) σ_{xx} — MF/CUF-HF

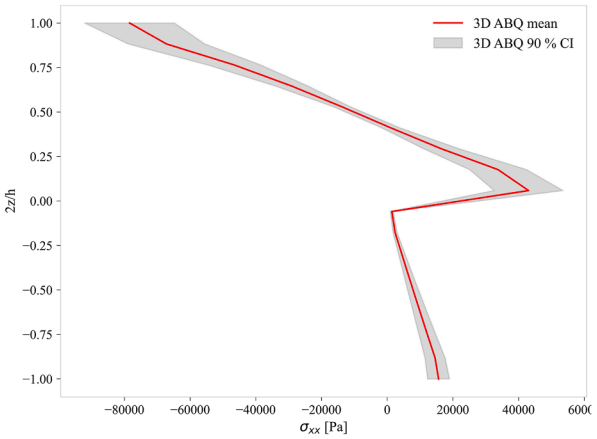

(b) σ_{xx} — Abaqus–3D

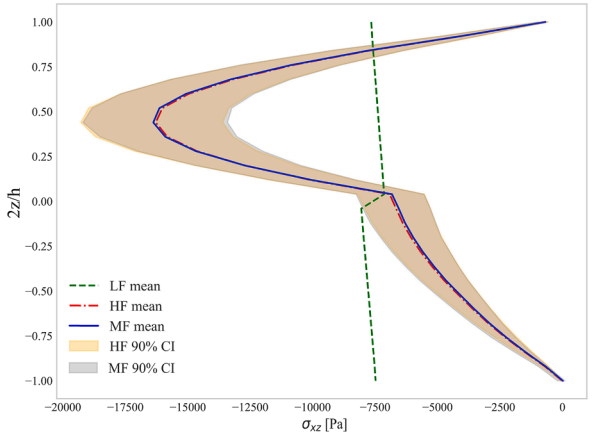

(c) σ_{xz} — MF/CUF-HF

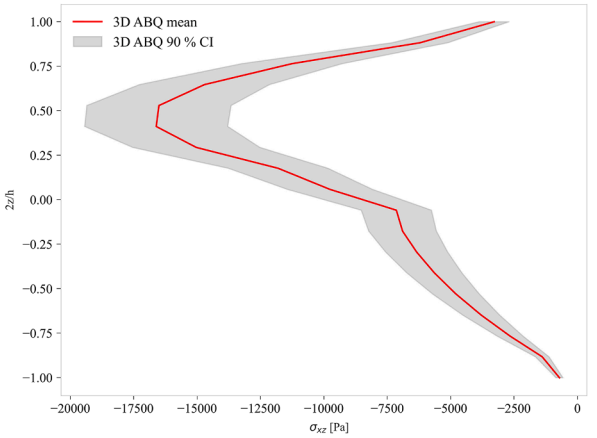

(d) σ_{xz} — Abaqus–3D

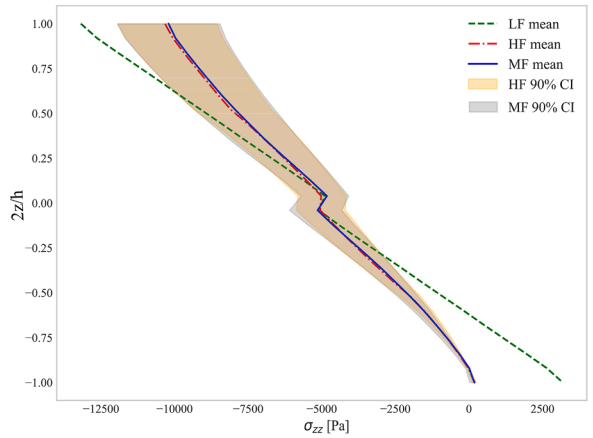

(e) σ_{zz} — MF/CUF-HF

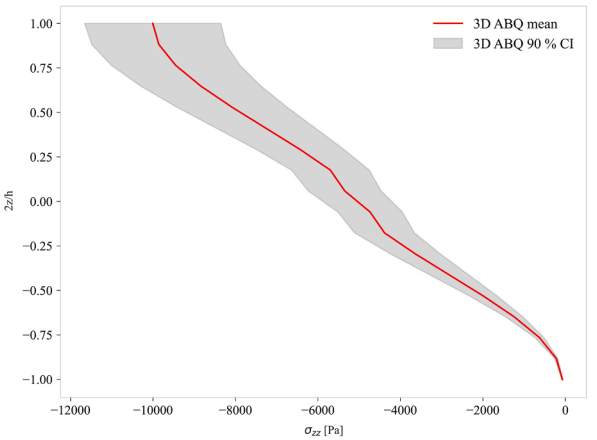

(f) σ_{zz} — Abaqus–3D

Fig. 8. Stresses through thickness under material and load uncertainty. Left column: LF/HF/MF mean with 90% CI (MC–HF, GPR–MF). Right column: MC–HF (3D Abaqus) reference.

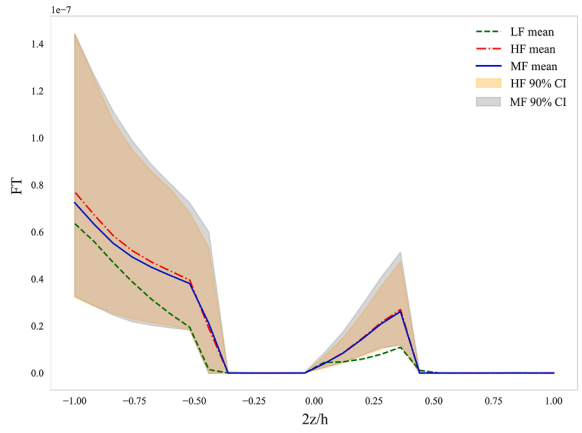

(a) FT — MF/CUF-HF

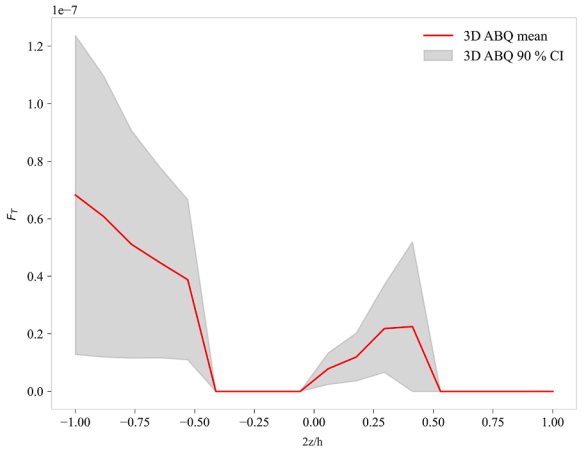

(b) FT — Abaqus–3D

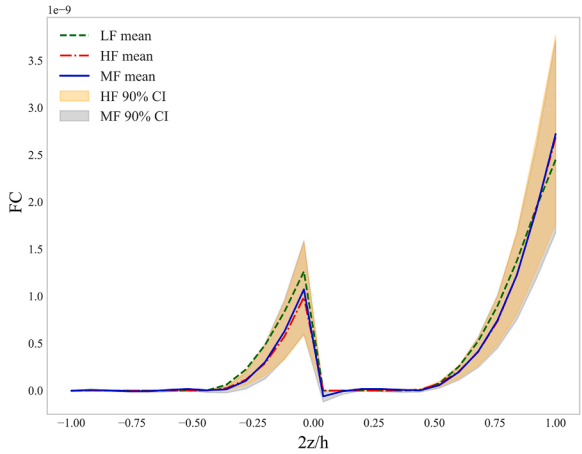

(c) FC — MF/CUF-HF

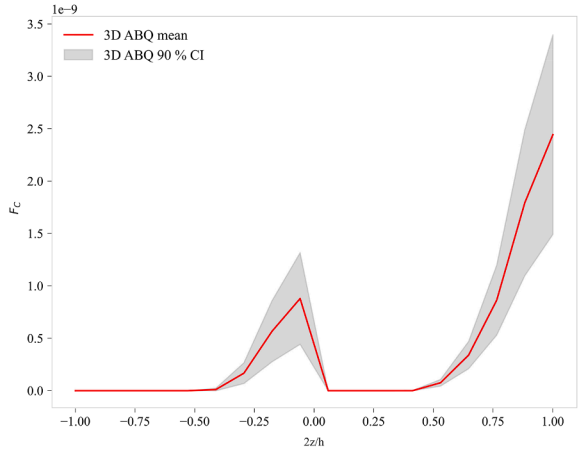

(d) FC — Abaqus–3D

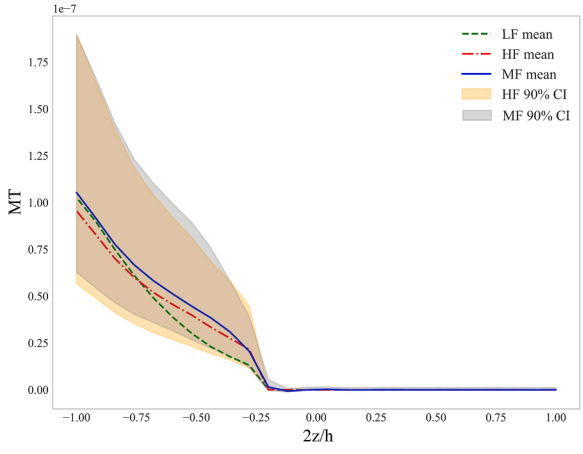

(e) MT — MF/CUF-HF

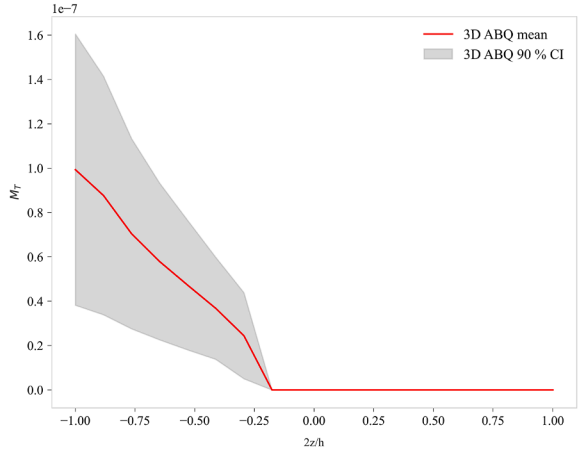

(f) MT — Abaqus–3D

Fig. 9. Failure indices along thickness under material and load uncertainty. Left column: LF/HF/MF mean with 90% CI (MC–HF, GPR–MF). Right column: MC–HF (3D Abaqus) reference.

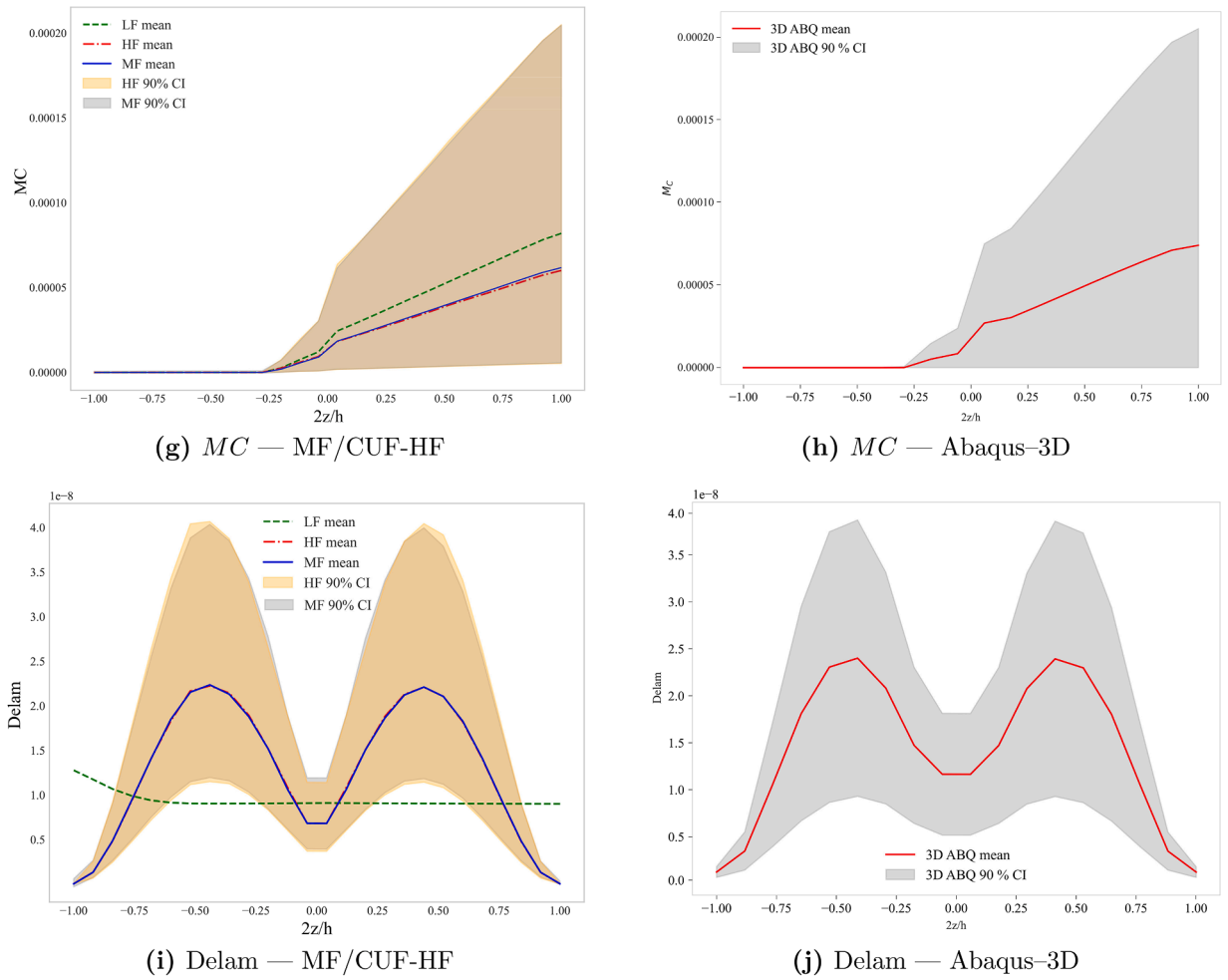

(g) MC — MF/CUF-HF (h) MC — Abaqus–3D

(i) Delam — MF/CUF-HF (j) Delam — Abaqus–3D

Fig. 9. Failure indices along thickness under material and load uncertainty. Left column: LF/HF/MF mean with 90% CI (MC–HF, GPR–MF). Right column: MC–HF (3D Abaqus) reference.

Table 6
MF performance metrics for the free-edge case. The total computational time refers to the complete execution of the GPR-MF framework, while S_{CUF} indicates the corresponding speedup with respect to the MC-HF simulations performed with CUF. The equal-cost confidence-envelope factor F_{CI} is also reported.

	Performance metrics							Computational cost	
Output	N_{LF}	N_{HF}	%HF	R^2	nRMSE	F_{CI}	MC-HF	T_{MF} [min]	S_{CUF}
Stresses (free-edge)									
$\sigma_{yz}/\varepsilon_{yy}$ (along x)	350	40	11.4%	0.997	0.008	1.70	400	17.7	2.54
$\sigma_{yz}/\varepsilon_{yy}$ (through z)	250	40	16.0%	0.998	0.006	1.82	400	14.0	3.22

- The quantitative metrics in Table 6 confirm the high predictive accuracy ($R^2 > 0.99$, nRMSE< 1%) and the computational efficiency of the MF model in capturing the complex stress state, achieved using 16% of HF evaluations. Compared to the previous case study, which required a larger number of HF simulations for shear components, the present configuration exhibits narrower and simpler uncertainty bands, thereby reducing the amount of HF data needed for training. In this case, a large LF dataset corrected by a small fraction of HF samples is sufficient to accurately recover the stress distribution under the aforementioned uncertainties.
- To compare MF-GPR against MC-HF under the same computational budget, Table 6 reports the equal-cost confidence-envelope factor F_{CI} (defined in Section 4.2). Under same computiational cost, MF-GPR reduces the confidence-envelope error by about +70% for $\sigma_{yz}/\varepsilon_{yy}$ evaluated along x, and by about +82% for the corresponding profile evaluated through z. The companion variability factor F_{σ}, also introduced in Section 4.2, indicates improvements of approximately +89% and +110% for the along-x and through-z responses, respectively.

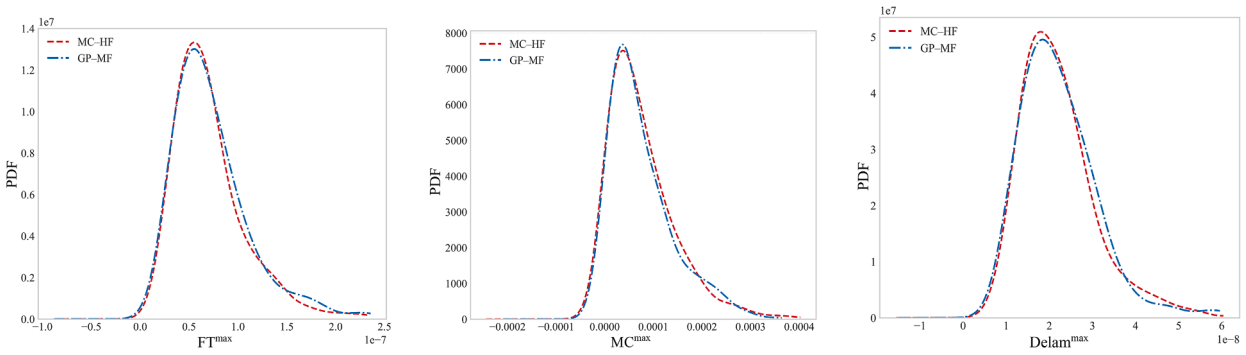

(a) FT (b) MC (c) Delam

Fig. 10. PDF of maximum failure indices across the thickness under material and load uncertainty. Comparison between MC-HF and GPR-MF.

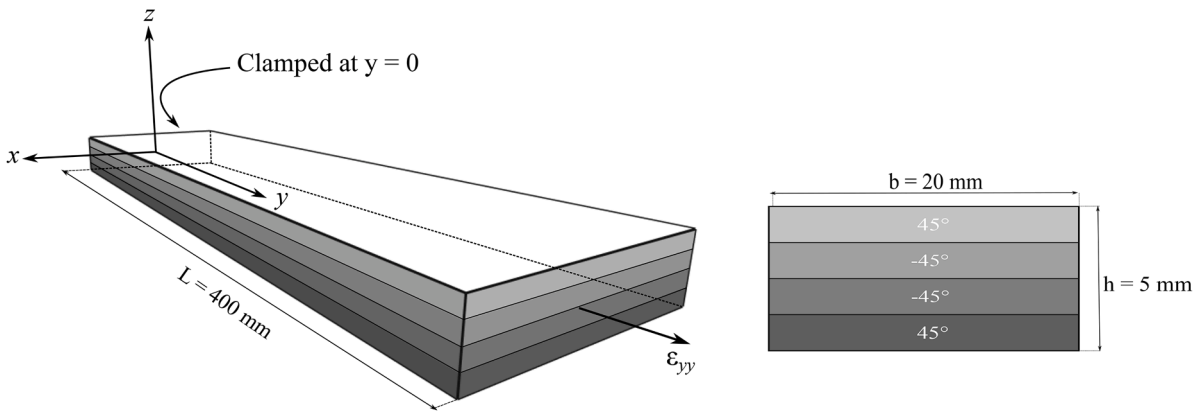

Fig. 11. Boundary conditions and loading of the laminate plate.

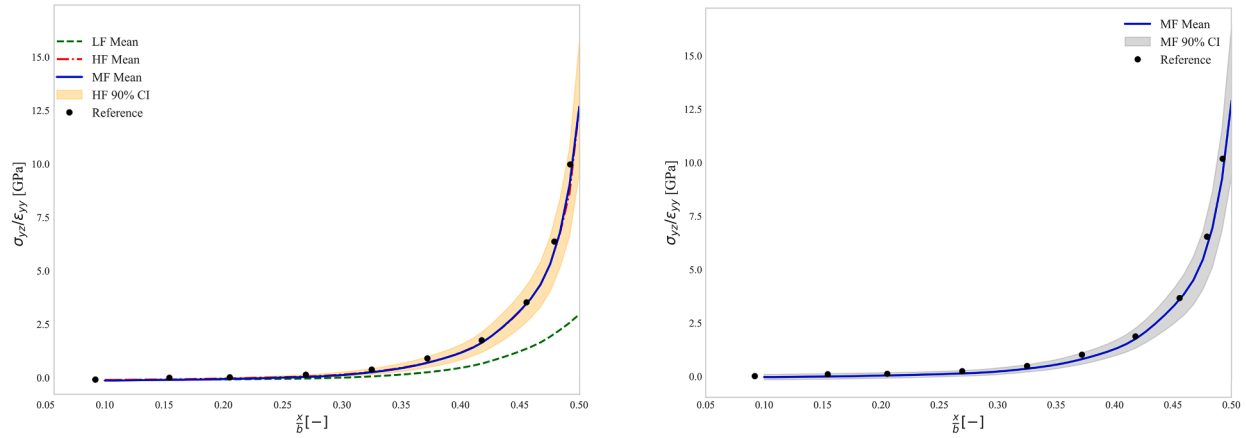

(a) Transverse shear stress σ_{xz} mean values of LF, HF, and MF models, with 90% CI from the HF model (CUF).

(b) Transverse shear stress σ_{xz} mean value and 90% CI from the adaptive MF-GPR surrogate.

Fig. 12. Transverse shear stress σ_{xz} along x at $z = h/4$ and $y = b/2$, with the x-axis starting from the free-edge and moving towards the plate center. Reference solution is taken from Wang and Crossman [102].

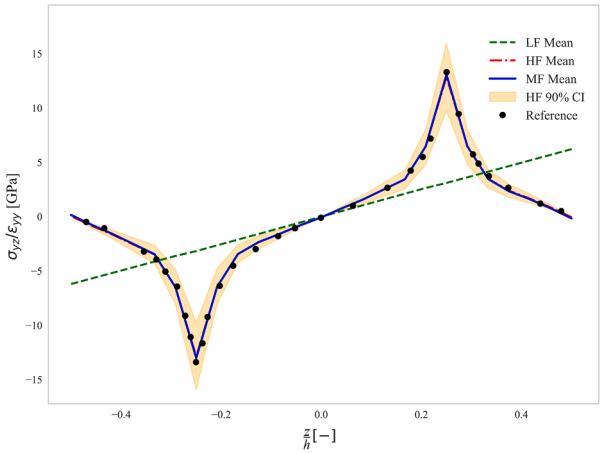

(a) Transverse shear stress σ_{xz} along z mean values of LF, HF, and MF models, with 90% CI from the HF model (CUF).

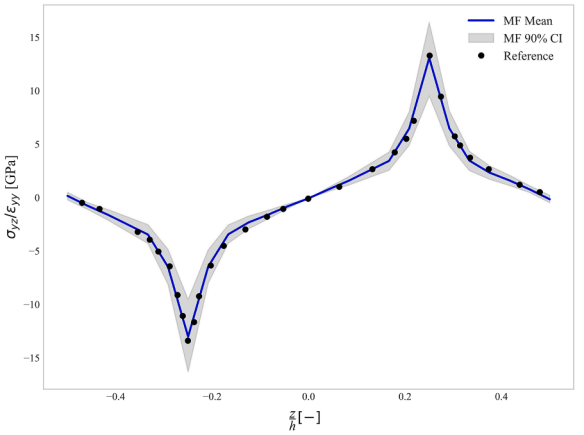

(b) Transverse shear stress σ_{xz} along z mean value and 90% CI from the adaptive MF-GPR surrogate.

Fig. 13. Transverse shear stress σ_{xz} along z at $y = L/2$ and $x = b$. Reference solution is taken from Wang and Crossman [102].

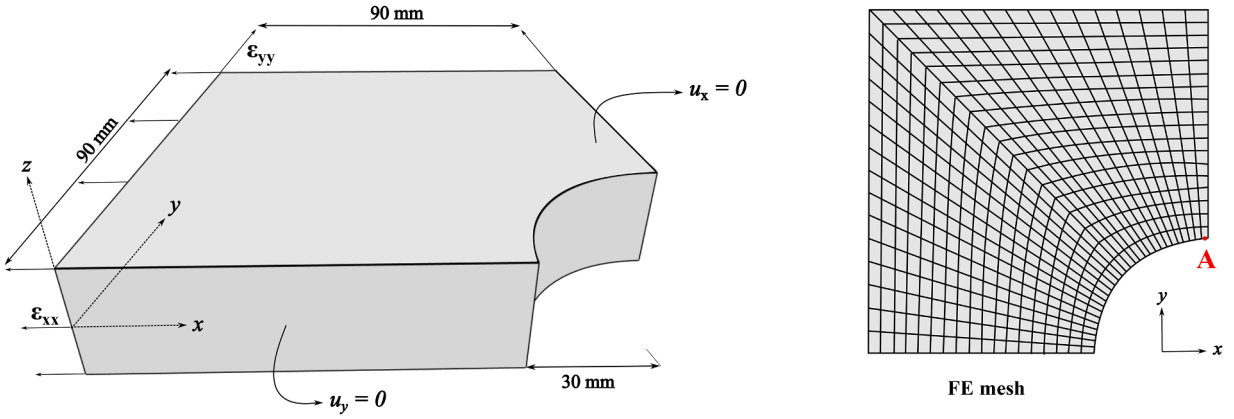

Fig. 14. Boundary conditions and loading of the open-hole composite plate.

4.4. *Probabilistic failure analysis of a composite open-hole plate*

This case study demonstrates the capability of the proposed MF framework to predict the probabilistic failure response of a composite plate with a central circular hole under tensile loading. The configuration adopted in this study corresponds to the benchmark case presented in Ref. Catapano and Montemurro [103], characterized by a symmetric laminate with stacking sequence $\theta = [45°/90°/-45°/0°]_{3s}$ and subjected to a uniform tensile load applied in the x and y direction. The geometry, boundary conditions, and applied load are shown in Fig. 14. Additionally, Fig. 14 illustrates the FE mesh adopted, chosen following the classical FE discretization recommended in [104] to balance computational cost and accuracy; in a higher-order FE context, however, a less detailed mesh would be admissible [42,105]. As in the previous case, Table 7 summarizes the statistical characterization of the material and load parameters, where the mean values correspond to the nominal mechanical properties and CoV quantifies their uncertainty. The elastic moduli, strength allowables, and applied pressure follow normal distributions, whereas the Poisson ratios are modeled as uniform random variables. In this study, the LF analyses are performed using an ESL model with TE1 expansion through the thickness (similar to FSDT as presented in the Ref. [103]) with 13542 DOF, while the HF analyses are based on a LW model with one LD1 expansion per ply (169275 DOF).

This section presents the probabilistic response of the open-hole plate in terms of through-thickness failure indices at the reference point A (see Fig. 14) in the proximity of the hole. Table 8 reports the MF performance and computational metrics for this case. Specifically, the average runtimes of the CUF low- and high-fidelity models are $t_{\mathrm{LF}} = 25.66$ s and $t_{\mathrm{HF}} = 71.05$ s, respectively. Fig. 15 display the probabilistic distributions of the Hashin 3D failure indices obtained through the laminate thickness, namely FT, FC, MT, and the delamination index. For each output it is reported (a) the CUF-based results by comparing the LF, HF, and MF mean curves and showing the 90% confidence interval associated with the HF simulations; and (b) the corresponding adaptive MF-GPR

Table 7
Statistical characterization of the material properties and applied loads for the open-hole composite plate.

Elastic properties			Strengths & load		
Parameter	Mean	CoV [%]	Parameter	Mean	CoV [%]
E_1 [GPa]	161	6.5	$\epsilon_{xx}, \epsilon_{yy}$ [–]	0.01	10.0
E_2 [GPa]	9.0	13.5	X_T [MPa]	1500	10.0
E_3 [GPa]	9.0	13.5	X_C [MPa]	1500	10.0
G_{12} [GPa]	6.1	13.0	Y_T [MPa]	40	15.0
G_{13} [GPa]	6.1	13.0	Y_C [MPa]	200	15.0
G_{23} [GPa]	6.1	13.0	S_{12} [MPa]	68	10.0
ν_{12} [–]	0.22–0.30	–	S_{13} [MPa]	40	10.0
ν_{13} [–]	0.22–0.30	–	S_{23} [MPa]	40	10.0
ν_{23} [–]	0.08–0.15	–	Z_T [MPa]	60	15.0

Table 8
Multi-fidelity performance metrics and computational indicators for the open-hole laminate. All quantities are evaluated along the thickness at point A. The equal-cost confidence-envelope factor F_{CI} is also reported. The total computational time refers to the complete execution of the GPR-MF framework, while S_{CUF} indicates the corresponding speedup with respect to the MC-HF simulations performed with CUF.

	Performance metrics							Computational cost	
Output	N_{LF}	N_{HF}	%HF	R^2	nRMSE	F_{CI}	MC-HF	T_{MF} [min]	S_{CUF}
Failure indices (open-hole)									
FT	700	83	11.9%	0.998	0.007	1.51	800	397.6	2.38
FC	550	40	7.3%	0.999	0.007	2.89	800	282.6	3.35
MT	500	150	30.0%	1.000	0.003	2.22	800	391.5	2.42
delam	550	300	54.5%	1.000	0.005	1.20	800	590.5	1.60

prediction, with the mean profile together with the 90% confidence interval obtained from the trained surrogate under the same uncertainty conditions. The matrix-compression failure index is not reported because it remains negligible under the present loading configuration.
From the results shown, the following comments can be drawn:

- All MF surrogates achieve good agreement with the MC-HF benchmarks ($R^2 \geq 0.998$, nRMSE ≤ 0.007 for FT/FC and ≤ 0.005 for MT/delam), while significantly reducing the computational cost, as seen in Table 8.
- Table 8 reports also the equal-cost confidence-envelope factor F_{CI} for the comparison between MF-GPR and MC-HF under the same computational budget. MF-GPR reduces the confidence-envelope error by about +51% for FT, +189% for FC, +122% for MT, and +20% for delamination. The companion variability factor F_σ indicates corresponding improvements of approximately +47%, +110%, +78%, and +15%, respectively.
- For the Fiber compression/tension indices (see Fig. 15a, b, c, d), the LF model already captures their through-thickness trends, and consequently the MF surrogate only needs a low number of HF corrections. In the plots, the MF mean overlaps the HF curve, and the MF CI adheres to the HF band across the thickness.
- The matrix-tension index (see Fig. 15e and f) is sensitive to transverse shear and through-the-thickness stress near the hole (see Appendix A). In fact, the LF model shows larger discrepancies with respect to the HF. The adaptive MF allocates more HF samples (30%), improving the LF prediction and matching both HF mean and CI.
- The delamination index (see Fig. 15g and h) depends on out-of-plane stresses, thus the LF model underpredicts the value and variability in the z direction, so the MF strategy must learn a larger, non-linear correction. In this case, 54.5% HF is needed. This matches the HF results but increases the computational cost ($S_{\mathrm{CUF}} = 1.45$).

To complement the mean and 90% confidence-interval profiles reported in Fig. 15 and the performance indicators in Table 8, a reliability measure is additionally evaluated within the same uncertainty framework. For a given failure mode k, the probability of failure onset is defined as:

$$P_{f,k} = \mathbb{P}\big(FI_{k,\max}(\mathbf{x}) \geq 1\big), \qquad FI_{k,\max}(\mathbf{x}) = \max_{\zeta \in [0,1]} FI_k(\mathbf{x}, \zeta), \tag{34}$$

where $\mathbf{x}$ denotes the vector of stochastic input parameters and ζ is the normalized through-thickness coordinate. In the present open-hole configuration, non-negligible probabilities of failure are observed for the FT and MT modes (consistent with the distributions in Fig. 15), whereas all other failure indices remain strictly below the critical threshold.
Based on the converged MC–HF baseline ($N = 800$), the reference failure probabilities are established as $P_{f,FT} = 2.50\%$ and $P_{f,MT} = 36.38\%$ The corresponding MF–GPR estimates, derived using the specific HF analyses detailed in Table 8 ($N_{HF} = 83$ for FT and $N_{HF} = 150$ for MT), result in $P_{f,FT} = 2.52\%$ and $P_{f,MT} = 36.20\%$, corresponding to relative deviations of 0.86% and 0.48%, respectively. To illustrate the through-thickness distribution, Fig. 16 reports the 3D layerwise probability of failure for matrix-tension onset,

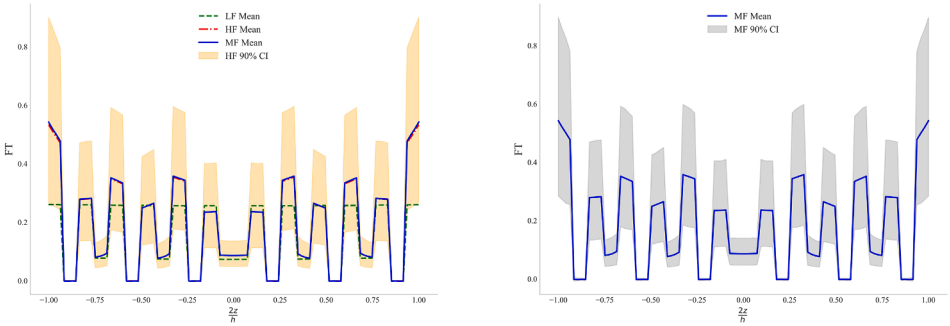

(a) FT with MC-HF CI.

(b) FT with MF–GPR CI.

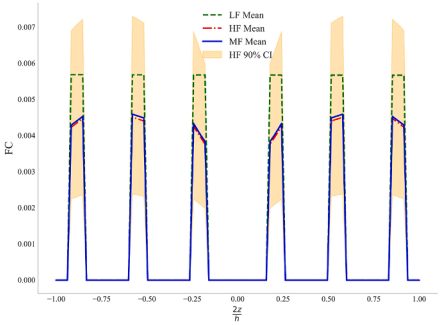

(c) FC with MC-HF CI.

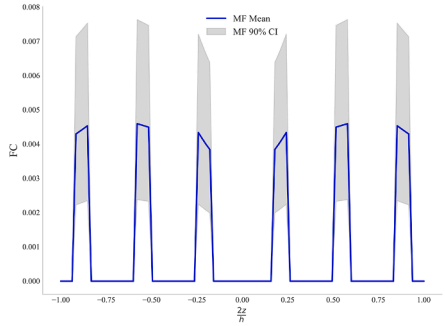

(d) FC with MF-GPR CI.

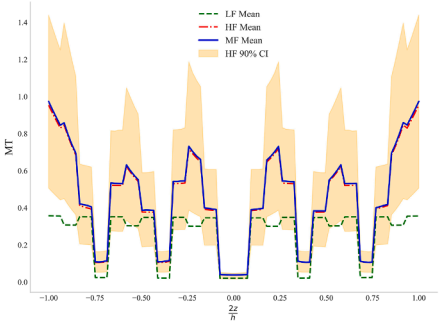

(e) MT with MC-HF CI.

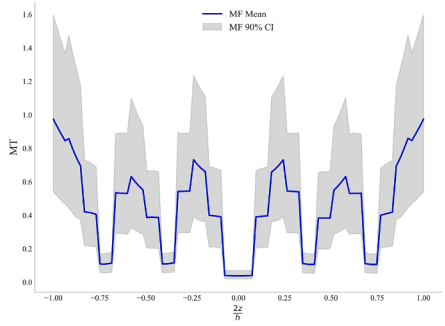

(f) MT with MF-GPR CI.

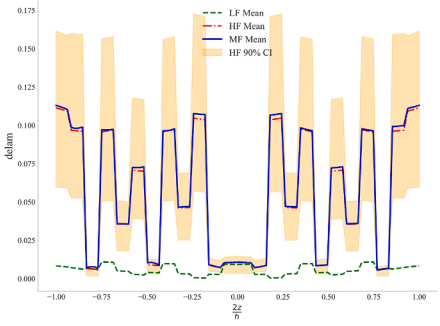

(g) Delamination with MC-HF CI.

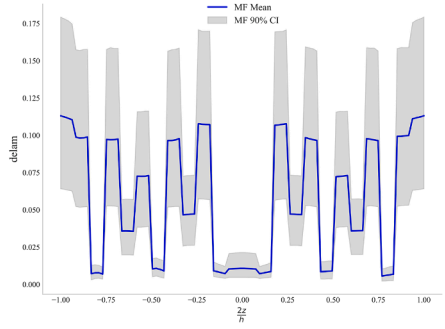

(h) Delamination with MF–GPR CI.

Fig. 15. MF-GPR results for the open-hole configuration. Left column reports LF, HF, and MF mean values with CUF-based HF confidence intervals, while right columns show the adaptive MF-GPR surrogate predictions with associated uncertainty.

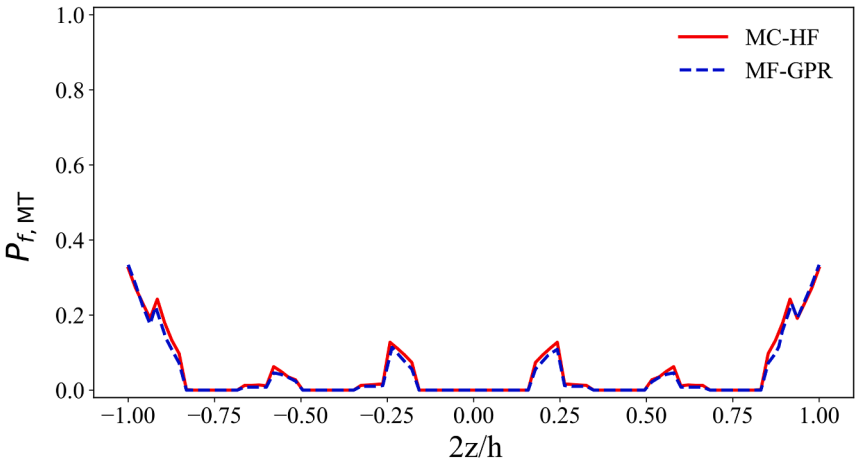

Fig. 16. Through-thickness probability of matrix-tension failure onset at point A for the open-hole configuration. Comparison between the converged MC–HF benchmark and the MF–GPR surrogate.

comparing the converged MC–HF benchmark and the proposed MF–GPR surrogate:

$$P_{f,MT}(z) = \mathbb{P}\big(FI_{MT}(\mathbf{x}, z) \geq 1\big) \tag{35}$$

This profile directly identifies the through-thickness regions that govern the probability of failure onset under the prescribed material and load uncertainties.

5. Conclusions

This work presented a MF framework based on probabilistic machine learning to analyze the propagation of uncertainties in composite structures. The objective is to determine the optimal number and distribution of LF and HF samples required to achieve accurate uncertainty estimates with minimal computational cost. The framework integrates low-fidelity ESL models and high-fidelity LW CUF models based on Taylor and Lagrange expansions through the thickness, respectively, exploiting their discrepancy to build an accurate and computationally efficient surrogate. CUF was utilized due to its versatility in generating different structural theories without the need for remeshing or rewriting the governing equations of the structural problem, making the integration of LF and HF models straightforward [106]. An adaptive active-learning strategy selects new HF samples based on epistemic uncertainty to reach convergence with a minimal number of expensive simulations. In this context, the use of LW models is essential, as they provide an accurate layerwise representation of the kinematic fields and enable the recovery of realistic through-thickness stress distributions, ensuring reliable identification of failure onset.

- The MF surrogate accurately reproduces the mean and CI of the 3D stress components and Hashin failure indices under material and load uncertainties for the composite plate (Figs. 8 and 9). The predictive distributions (PDF) of MF and HF nearly coincide, confirming statistical consistency (see Fig. 10). The highest sensitivity to uncertainty is observed for the out-of-plane stresses (σ_{xz},σ_{yz},σ_{zz}) and for the FT, MC, and delamination indices, whereas the in-plane stresses (σ_{xx},σ_{yy},σ_{xy}), MT and FC show narrower confidence bands. As reported in Table 3, the adaptive strategy converges with about 20–300 HF evaluations, against 600 MC-HF simulations required by the benchmark. In contrast, the non-adaptive MF (see Appendix B) fails to recover the HF confidence bands near the laminate surfaces due to limitations of the underlying ESL-TE1 model. In addition, the performance assessment at a fixed computational budget (see Table 3) confirms that MF-GPR significantly refines the 90% confidence envelope and of the through-thickness variability profile, with typical gains of about 45–120% for F_{CI} and 16–110% for F_{σ} depending on the output.
- The discrepancy between the ESL and LW models becomes more pronounced near the edges due to strong interlaminar stress variations. ESL models fail to reproduce the local stress state of the shear components, leading to discrepancies that the MF-GPR efficiently corrects. Despite this modeling gap, the uncertainty bands remain narrow (Figs. 12 and 13), indicating limited sensitivity to input variability; hence, only a small fraction of HF data is required. Specifically, convergence is achieved with 40 HF simultations, compared to about 400 MC–HF evaluations required by the benchmark (see Table 6). The comparison at the same computational cost (see Table 6) yields confidence-envelope improvements of about +70% and +82% for the along-x and through-z responses, respectively, with corresponding variability-profile improvements of approximately +89% and +110%.
- For the open-hole configuration, the largest CI widths are observed for the MT and delamination indices, which require more HF analyses to achieve accurate probabilistic reconstruction (Fig. 15). In this case as well, adaptive learning is essential for the MF predictions to reproduce the HF mean and CI profiles, yielding a substantial reduction in computational cost. In particular, convergence is reached with 40–300 HF simulations, compared to 800 MC-HF runs required by the reference benchmark, thus yielding a substantial reduction in computational cost (see Table 8). Moreover, the assessment at the same computational cost reported in Table 8 indicates that, the confidence-envelope error is reduced by about +51% for FT, +189% for FC, +122% for

MT, and +20% for delamination, with corresponding variability-profile improvements of approximately +47%, +110%, +78%, and +15%, respectively.

- The proposed MF framework quantifies uncertainty for fully three-dimensional, layerwise stress fields and failure indices. This enables the definition of reliability indicators for spatially distributed responses, providing location-dependent probabilities of failure and allowing critical plies or interfaces to be identified under uncertainties, rather than relying solely on global maxima [107]. Furthermore, the reconstruction of full layerwise profiles enables the use of continuous metrics based on thickness integration. Unlike discrete max-type criteria, these formulations produce smooth responses that are inherently compatible with gradient-based optimization. The open-hole results confirm that the governing onset probabilities and the through-the-thickness probability profile are accurately reproduced by MF–GPR with respect to the converged MC–HF benchmark (see Fig. 16).

In conclusion, the proposed framework proved robust and computationally efficient, successfully capturing the propagation of material and load uncertainties across multiple composite configurations. Nevertheless, probabilistic assessments require prior knowledge of the input probability distributions, which are often unavailable or only partially characterized. Moreover, the MF accuracy depends on the discrepancy between the LF and HF models and may require localized corrections in highly nonlinear regions. The aggregate computational time of LF and HF evaluations can also become non-negligible when HF analyses are particularly expensive or when adaptive enrichment converges slowly. Despite these limitations, the framework maintains high predictive accuracy while reducing computational demands, yielding statistically consistent uncertainty propagation. Future investigations will extend the methodology to progressive failure and geometrically nonlinear problems under uncertainties, and to Reliability-Based Design Optimization (RBDO) to embed uncertainty quantification directly into CUF-based structural optimization.

CRediT authorship contribution statement

D. Zamani: Writing – original draft, Validation, Methodology, Investigation, Formal analysis, Conceptualization; **A. Pagani:** Writing – review & editing, Supervision, Methodology, Funding acquisition, Conceptualization; **M. Petrolo:** Writing – review & editing, Supervision, Methodology, Conceptualization; **E. Carrera:** Writing – review & editing, Supervision, Methodology, Conceptualization.

Data availability

Data will be made available on request.

Declaration of competing interest

The authors declare that they have no known competing financial interests or personal relationships that could have appeared to influence the work reported in this paper.

Acknowledgment

The support of the Italian Ministry of University and Research through the program FARE-III Edition (project LOUD, No. R20EENHZEJ) is acknowledged.

Appendix A. Hashin 3D and delamination failure criteria

The failure indices used to assess the structural integrity of the composite laminate are based on the Hashin 3D failure criteria [108]. The formulations for fiber tension (FT), fiber compression (FC), matrix tension (MT), and matrix compression (MC) are given by:

- Fiber tension ($\sigma_{11} \geq 0$):

$$FT = \left(\frac{\sigma_{11}}{X_T}\right)^2 + \frac{\sigma_{12}^2 + \sigma_{13}^2}{S_{12}^2} \geq 1 \tag{A.1}$$

- Fiber compression ($\sigma_{11} < 0$):

$$FC = \left(\frac{\sigma_{11}}{X_C}\right)^2 \geq 1 \tag{A.2}$$

- Matrix tension ($\sigma_{22} + \sigma_{33} \geq 0$):

$$MT = \frac{(\sigma_{22} + \sigma_{33})^2}{Y_T^2} + \frac{\sigma_{23}^2 - \sigma_{22}\sigma_{33}}{S_{23}^2} + \frac{\sigma_{12}^2 + \sigma_{13}^2}{S_{12}^2} \geq 1 \tag{A.3}$$

- Matrix compression ($\sigma_{22} + \sigma_{33} < 0$):

$$MC = \left[\left(\frac{Y_C}{2S_{23}}\right)^2 - 1\right]\left(\frac{\sigma_{22} + \sigma_{33}}{Y_C}\right)$$

$$+\frac{(\sigma_{22}+\sigma_{33})^2}{4S_{23}^2}+\frac{\sigma_{23}^2-\sigma_{22}\sigma_{33}}{S_{23}^2}+\frac{\sigma_{12}^2+\sigma_{13}^2}{S_{12}^2}\geq 1 \tag{A.4}$$

Here, σ_{ij} are the components of the stress tensor in the material coordinate system, where direction 1 corresponds to the fiber direction, while 2 and 3 represent the transverse directions. X and Y denote the material strengths, with subscripts T and C indicating tension and compression, respectively. S_{ij} represent the material shear strengths. A failure is predicted when any index value is greater than or equal to one.

Additionally, delamination index is considered as well, since this failure mechanism has proven to be of major concern when considering manufacturing defects [109,110]. The delamination index is calculated by means of the mixed mode quadratic criterion [111], given by the following equation:

$$Delam=\left(\frac{\langle\sigma_{33}\rangle}{Z_T}\right)^2+\left(\frac{\sigma_{23}}{S_{23}}\right)^2+\left(\frac{\sigma_{13}}{S_{13}}\right)^2\geq 1 \tag{A.5}$$

where $\langle\sigma_{33}\rangle$ denotes the $\max(0,\sigma_{33})$, Z_T is the transverse tensile strength through the thickness direction, and S_{23} and S_{13} are the transverse shear strengths. Delamination is assumed to occur when this index reaches or exceeds unity.

Appendix B. Non-adaptive MF–GPR result

This appendix presents a comparison between the non-adaptive MF-GPR and the adaptive MF-GPR baseline for Section 4.2, both evaluated at the same computational cost. For completeness, Fig. B.17 summarizes the sequence of HF acquisitions produced by adaptive learning in Section 4.2, clarifying how the HF budget is progressively allocated for the delamination index (see Table 3).

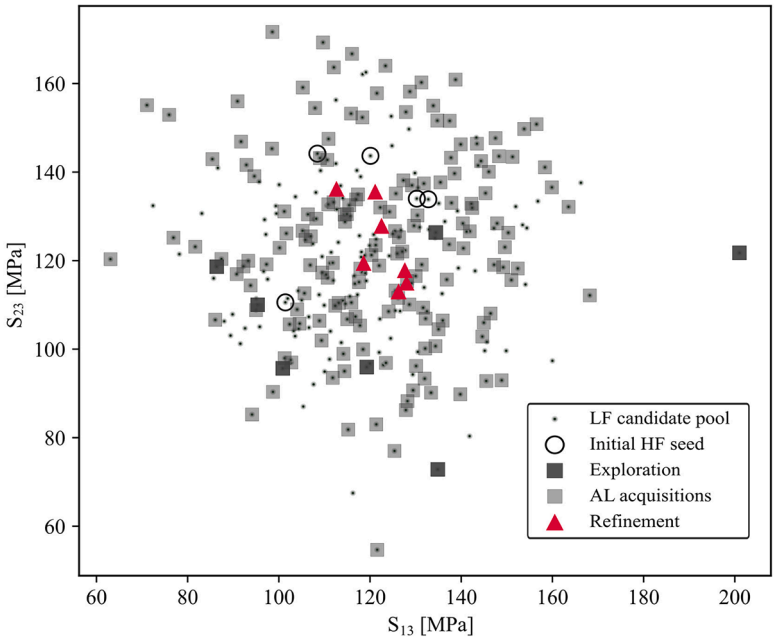

Fig. B.17. Adaptive HF sampling sequence for the delamination index in Section 4.2, shown as a projection in the input uncertainty space (S_{13}, S_{23}). Gray dots denote the LF candidate pool U_j; Open circles indicate the initial HF set $D_{H,0}$, randomly selected from the LF candidate pool U_j, while filled squares represent the HF samples added by adaptive learning; and red triangles highlight the final refinement. As reported in Table 3, this output uses $N_{LF}=400$ LF evaluations (i.e., the size of U_j) and $N_{HF}=300$ HF evaluations in total. (For interpretation of the references to colour in this figure legend, the reader is referred to the web version of this article.)

Fig. B.18 presents the predictions generated by the non-adaptive GPR-MF surrogate for the case study described in Section 4.2. For each quantity, the figure provides the mean curve and the 90% confidence interval, both evaluated through the thickness under material and load uncertainty. Specifically, for the out-of-plane normal and transverse shear components σ_{zz}, σ_{xz} and σ_{yz} (see Fig. B.18b, c) and for the delamination index (Fig. B.18h), the non-adaptive GPR-MF surrogate does not reproduce the HF confidence bands at the laminate boundaries. This limitation aligns with the characteristics of the LF model, namely the ESL-TE1 formulation (similar to FSDT), which typically neglects the C_z^0 continuity requirements and fails to enforce three-dimensional equilibrium pointwise, leading to inaccuracies near the top and bottom surfaces of the plate. In contrast, for quantities where the LF–HF mismatch is milder, such as the in-plane stress σ_{xx} and the fiber/matrix failure indices FT, FC, MT, and MC (see Fig. B.18a, c, d, e, f), the difference between adaptive and non-adaptive GPR–MF is minimal.

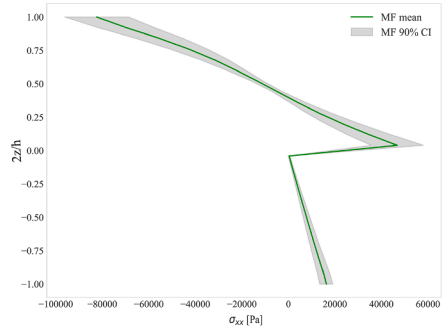

(a) σ_{xx} - GPR–MF non-adaptive.

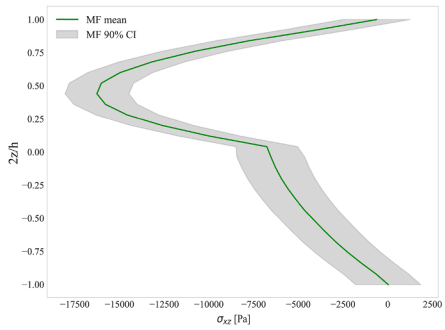

(b) σ_{xz} - GPR–MF non-adaptive.

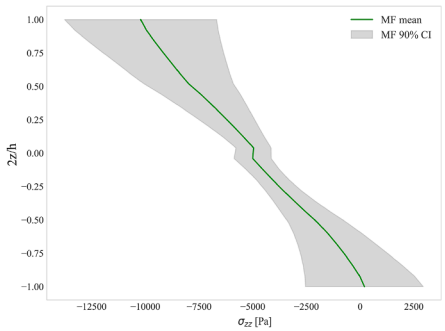

(c) σ_{zz} - GPR–MF non-adaptive.

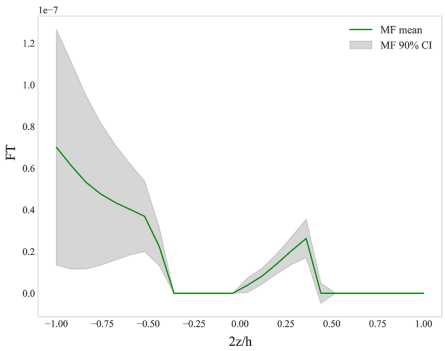

(d) FT - GPR–MF non-adaptive.

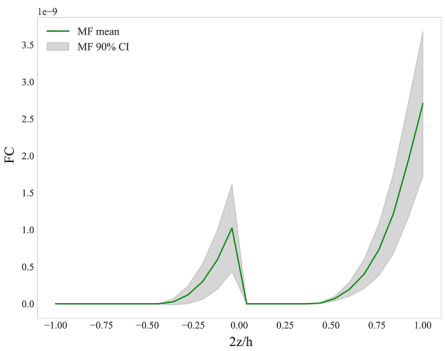

(e) FC - GPR–MF non-adaptive.

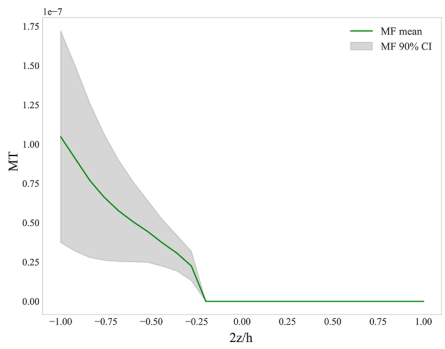

(f) MT - GPR–MF non-adaptive.

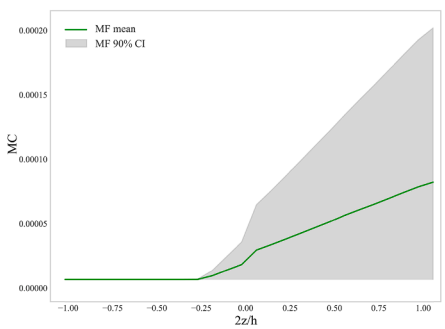

(g) MC - GPR–MF non-adaptive.

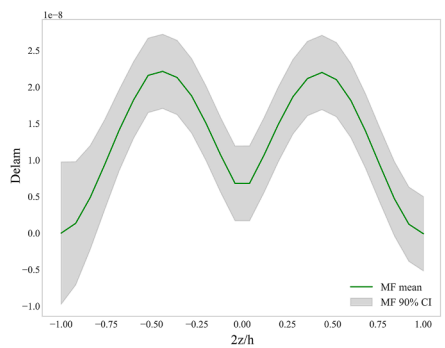

(h) Delam - GPR–MF non-adaptive.

Fig. B.18. Non-adaptive GPR–MF predictions with mean value and 90% CI.

References

[1] S.W. Tsai, Composites Design, Think Composites, Dayton, 4th edition, Dayton, 1988.
[2] C. Zweben, Composite Materials, John Wiley & Sons, Ltd, 2015, pp. 1–37.
[3] E.J. Pineda, A.M. Waas, B.A. Bednarcyk, et al., Progressive damage and failure modeling in notched laminated fiber reinforced composites, Int. J. Fract. 158 (2009) 125–143. https://doi.org/10.1007/s10704-009-9370-3
[4] Y. Liu, J. Xie, X. Chen, et al., Characterization of progressive damage behaviour and failure mechanism of carbon fiber reinforced composite laminates, Sci. Rep. 15 (2025) 13791. https://doi.org/10.1038/s41598-025-98774-7
[5] R.V. Wagenen, A Guide to Structural Factors for Advanced Composites Used on Spacecraft, Technical Report CR-186010, NASA, 1989. August.
[6] Z. del Rosario, R.W. Fenrich, G. Iaccarino, When are allowables conservative?, AIAA J. 59 (2021) 1760–1772. https://doi.org/10.2514/1.J059578
[7] Z. Duan, Y. Jung, J. Yan, et al., Reliability-based multi-scale design optimization of composite frames considering structural compliance and manufacturing constraints, Struct. Multidiscip. Optim. 61 (2020) 2401–2421. https://doi.org/10.1007/s00158-020-02517-3
[8] P. Hao, H. Yang, Y. Wang, X. Liu, B. Wang, G. Li, Efficient reliability-based design optimization of composite structures via isogeometric analysis, Reliab. Eng. Syst. Saf. 209 (2021) 107465. https://doi.org/10.1016/j.ress.2021.107465
[9] A. Racionero Sánchez-Majano, A. Pagani, Reliability-based design optimization of tow-steered composite plates employing high-order CUF-based finite elements, in: AIAA SCITECH 2022 Forum, 2022. https://api.semanticscholar.org/CorpusID:245737133.
[10] M.H. Hassan, A.R. Othman, S. Kamaruddin, A review on the manufacturing defects of complex-shaped laminate in aircraft composite structures, Int. J. Adv. Manuf. Technol. 91 (2017) 4081–4094. https://doi.org/10.1007/s00170-017-0096-5
[11] F. Heinecke, C. Willberg, Manufacturing-induced imperfections in composite parts manufactured via automated fiber placement, J. Composit. Sci. 3 (2019) 56. https://doi.org/10.3390/jcs3020056
[12] Y. Fu, X. Yao, A review on manufacturing defects and their detection of fiber reinforced resin matrix composites, Composit. Part C Open Access 8 (2022) 100276. https://doi.org/10.1016/j.jcomc.2022.100276
[13] M. Mehdikhani, L. Gorbatikh, I. Verpoest, S.V. Lomov, Voids in fiber-reinforced polymer composites: a review on their formation, characteristics, and effects on mechanical performance, J. Compos. Mater. 53 (2019) 1579–1669. https://doi.org/10.1177/0021998318772152
[14] X. Li, S. Shonkwiler, S. McMains, Detection of resin-rich areas for statistical analysis of fiber-reinforced polymer composites, Composit. Part B Eng. 225 (2021) 109252. https://doi.org/10.1016/j.compositesb.2021.109252
[15] M.P. Alves, C.A. Cimini Junior, S.K. Ha, Fiber waviness and its effect on the mechanical performance of fiber reinforced polymer composites: an enhanced review, Compos. Part A Appl. Sci. Manufact. 149 (2021) 106526. https://doi.org/10.1016/j.compositesa.2021.106526
[16] M. Jafarypouria, S.V. Lomov, B. Mahato, S.G. Abaimov, The effect of fibre misalignment in an impregnated fibre bundle on stress concentrations, Compos. Part A Appl. Sci. Manufact. 178 (2024) 108001. https://doi.org/10.1016/j.compositesa.2023.108001
[17] A.F. Gill, P. Robinson, S. Pinho, Effect of variation in fibre volume fraction on modes I and II delamination behaviour of 5HS woven composites manufactured by RTM, Compos. Sci. Technol. 69 (2009) 2368–2375. https://doi.org/10.1016/j.compscitech.2009.02.008
[18] R.E. Caflisch, Monte Carlo and quasi-Monte Carlo methods, Acta Numerica 7 (1998) 1–49. https://doi.org/10.1017/S0962492900002804
[19] J.C. Helton, J.D. Johnson, C.J. Sallaberry, C.B. Storlie, Survey of sampling-based methods for uncertainty and sensitivity analysis, Reliab. Eng. Syst. Saf. 91 (10) (2006) 1175–1209. https://doi.org/10.1016/j.ress.2005.11.017
[20] C.E. Rasmussen, C.K.I. Williams, Gaussian Processes for Machine Learning, The MIT Press, Cambridge, MA, USA, Cambridge, MA, USA, 2005.
[21] M. Kanagawa, P. Hennig, D. Sejdinovic, B.K. Sriperumbudur, Gaussian Processes and Kernel Methods: A Review on Connections and Equivalences, arXiv preprint arXiv:1807.02582 (2018).
[22] M. Wynn, N. Zobeiry, Investigating the effect of temperature history on crystal morphology of thermoplastic composites using in situ polarized light microscopy and probabilistic machine learning, Polymers 15 (1) (2023) 18. https://doi.org/10.3390/polym15010018
[23] Y. Freed, M. Salviato, N. Zobeiry, Implementation of a probabilistic machine learning strategy for failure predictions of adhesively bonded joints using cohesive zone modeling, Int. J. Adhes. Adhes. 118 (2022) 103226. https://doi.org/10.1016/j.ijadhadh.2022.103226
[24] Y. Freed, N. Zobeiry, M. Salviato, Development of aviation industry-oriented methodology for failure predictions of brittle bonded joints using probabilistic machine learning, Compos. Struct. 297 (2022) 115979. https://doi.org/10.1016/j.compstruct.2022.115979
[25] H. An, B.D. Youn, H.S. Kim, Reliability-based design optimization of laminated composite structures under delamination and material property uncertainties, Int. J. Mech. Sci. 205 (2021) 106561. https://doi.org/10.1016/j.ijmecsci.2021.106561
[26] M.A. Bessa, S. Pellegrino, Design of ultra-thin shell structures in the stochastic post-buckling range using Bayesian machine learning and optimization, Int. J. Solids Struct. 139-140 (2018) 174–188. https://doi.org/10.1016/j.ijsolstr.2018.01.035
[27] K. Zhou, R. Enos, D. Zhang, J. Tang, Uncertainty analysis of curing-induced dimensional variability of composite structures utilizing physics-guided Gaussian process meta-modeling, Compos. Struct. 280 (2022) 114816. https://doi.org/10.1016/j.compstruct.2021.114816
[28] H. Teimouri, A.S. Milani, J. Loeppky, R. Seethaler, A Gaussian process-based approach to cope with uncertainty in structural health monitoring, Struct. Health Monit. 16 (2016) 174–184. https://doi.org/10.1177/1475921716669722
[29] J. Paixão, S. da Silva, E. Figueiredo, L. Radu, G. Park, Delamination area quantification in composite structures using Gaussian process regression and auto-regressive models, J. Vib. Control 27 (2020) 2778–2792. https://doi.org/10.1177/1077546320966183
[30] X. Yue, Y. Wen, J.H. Hunt, J. Shi, Active learning for Gaussian process considering uncertainties with application to shape control of composite fuselage, IEEE Trans. Autom. Sci. Eng. 18 (2021) 36–46. https://doi.org/10.1109/TASE.2020.2990401
[31] Q. Guo, J. Hang, S. Wang, et al., Design optimization of variable stiffness composites by using multi-fidelity surrogate models, Struct. Multidiscip. Optim. 63 (2021) 439–461. https://doi.org/10.1007/s00158-020-02684-3
[32] Z. Gürdal, R. Olmedo, In-plane response of laminates with spatially varying fiber orientations - variable stiffness concept, AIAA J. 31 (4) (1993) 751–758. https://doi.org/10.2514/3.11613
[33] A. Garg, S. Naskar, T. Mukhopadhyay, Elementary-level intrusive coupling of machine learning for efficient mechanical analysis of variable stiffness composite laminates: a spatially-adaptive fidelity-sensitive computational framework, Eng. Comput. 41 (2025) 2291–2318. https://doi.org/10.1007/s00366-024-02082-z.
[34] H. An, Y. Zhang, Q. Deng, T. Long, B.D. Youn, H.S. Kim, Integrated optimization of ply number, layer thickness, and fiber angle for variable-stiffness composites using dynamic multi-fidelity surrogate model, Thin-Walled Struct. 206 (2025) 112392. https://doi.org/10.1016/j.tws.2024.112392
[35] L.G. Ribeiro, E. Parente, A.M.C. de Melo, Alternative variable-fidelity acquisition functions for efficient global optimization of black-box functions, Struct. Multidiscip. Optim. 66 (2023) 147. https://doi.org/10.1007/s00158-023-03607-8
[36] K. Tian, J. Zhang, X. Ma, Y. Li, Y. Sun, P. Hao, Buckling surrogate-based optimization framework for hierarchical stiffened composite shells by enhanced variance reduction method, J. Reinf. Plast. Compos. 38 (2019) 959–973. https://doi.org/10.1177/0731684419862350
[37] M.-J. Li, Y. Lian, Z. Cheng, L. Li, Z. Wang, R. Gao, D. Fang, A clustering adaptive Gaussian process regression method: response patterns based real-time prediction for nonlinear solid mechanics problems, 2024, arXiv:2409.10572
[38] E. Carrera, Theories and finite elements for multilayered plates and shells: a unified compact formulation with numerical assessment and benchmarking, Arch. Comput. Methods Eng. 10 (2003) 215–296. https://doi.org/10.1007/BF02736224
[39] E. Carrera, G. Giunta, Hierarchical evaluation of failure parameters in composite plates, AIAA J. 47 (2009) 692–702. https://doi.org/10.2514/1.38585
[40] A. Pagani, A.G. de Miguel, M. Petrolo, E. Carrera, Analysis of laminated beams via unified formulation and legendre polynomial expansions, Compos. Struct. 156 (2016) 78–92. https://doi.org/10.1016/j.compstruct.2016.01.095
[41] P. Nali, E. Carrera, A numerical assessment on two-dimensional failure criteria for composite layered structures, Composit. Part B Eng. 43 (2012) 280–289. https://doi.org/10.1016/j.compositesb.2011.06.018
[42] A.G. de Miguel, I. Kaleel, M.H. Nagaraj, A. Pagani, M. Petrolo, E. Carrera, Accurate evaluation of failure indices of composite layered structures via various FE models, Compos. Sci. Technol. 167 (2018) 174–189. https://doi.org/10.1016/j.compscitech.2018.07.031

[43] E. Carrera, M. Cinefra, M. Petrolo, E. Zappino, Finite Element Analysis of Structures through Unified Formulation, Wiley, Hoboken, New Jersey, USA, Hoboken, New Jersey, USA, 2014.
[44] A. Pagani, E. Carrera, R. Augello, D. Scano, Use of Lagrange polynomials to build refined theories for laminated beams, plates and shells, Compos. Struct. 276 (2021) 114505. https://doi.org/10.1016/j.compstruct.2021.114505
[45] J.N. Reddy, Mechanics of Laminated Composite Plates and Shells: Theory and Analysis, CRC Press, Boca Raton, Florida, USA, Boca Raton, Florida, USA, 2004.
[46] A. Pagani, A.R. Sánchez-Majano, Influence of fiber misalignments on buckling performance of variable stiffness composites using layerwise models and random fields, Mech. Adv. Mater. Struct. 29 (3) (2020) 384–399. https://doi.org/10.1080/15376494.2020.1771485
[47] A.R. Sánchez-Majano, A. Pagani, M. Petrolo, C. Zhang, Buckling sensitivity of tow-steered plates subjected to multiscale defects by high-order finite elements and polynomial chaos expansion, Materials 14 (11) (2021) 2706. https://doi.org/10.3390/ma14112706
[48] M.H. Nagaraj, I. Kaleel, E. Carrera, M. Petrolo, Elastoplastic micromechanical analysis of fiber-reinforced composites with defects, Aerotecnica Missili & Spazio 101 (2022) 53–59. https://doi.org/10.1007/s42496-021-00103-4
[49] M. Petrolo, A. Pagani, M. Trombini, E. Carrera, Voids effect on micromechanical response of elastoplastic fiber-reinforced polymer composites using 1D higher-order theories, Mech. Mater. 184 (2023) 104747. https://doi.org/10.1016/j.mechmat.2023.104747
[50] M. Petrolo, A. Pagani, M. Trombini, R. Masia, E. Carrera, Thermomechanical analysis of carbon fiber-reinforced polymer representative volume elements with voids, J. Reinf. Plast. Compos. 43 (23-24) (2024) 1375–1392. https://doi.org/10.1177/07316844231206956
[51] A. Pagani, A. Racionero Sánchez-Majano, D. Zamani, M. Petrolo, E. Carrera, Fundamental frequency layer-wise optimization of tow-steered composites considering gaps and overlaps, Aerotecnica Missili & Spazio (2024) 1–17. https://doi.org/10.1007/s42496-024-00212-w
[52] A. Pagani, A. Racionero Sánchez-Majano, D. Zamani, Optimization of variable stiffness composites considering gaps/overlaps and unified structural theories, in: ASME Aerospace Structures, Structural Dynamics, and Materials Conference, American Society of Mechanical Engineers, 2024, p. 87745. https://doi.org/10.1115/SSDM2024-121550
[53] E. Snelson, Z. Ghahramani, C. Rasmussen, Warped Gaussian processes, in: Advances in Neural Information Processing Systems, 16, 2003.
[54] S. Pfingstl, C. Braun, A. Nasrollahi, F.-K. Chang, M. Zimmermann, Warped Gaussian processes for predicting the degradation of aerospace structures, Struct. Health Monit. 22 (4) (2022) 2531–2546. https://doi.org/10.1177/14759217221127252
[55] P. Colombo, C. Miller, X. Yang, R. O'Donnell, P. Maranzano, Warped multifidelity Gaussian processes for data fusion of skewed environmental data, J. R. Stat. Soc. Ser. C Appl. Stat. 74 (2025) 844–865. https://doi.org/10.1093/jrsssc/qlaf003
[56] M.C. Jones, A. Pewsey, Sinh–arcsinh distributions, Biometrika 96 (4) (2009) 761–780. https://doi.org/10.1093/biomet/asp053
[57] X. Li, Q. Yang, Y. Wang, X. Han, Y. Cao, L. Fan, J. Ma, Development of surrogate models in reliability-based design optimization: a review, Math. Biosci. Eng. 18 (2021) 6386–6409. https://doi.org/10.3934/mbe.2021317
[58] Z. Azarhoosh, M. Ilchi Ghazaan, A review of recent advances in surrogate models for uncertainty quantification of high-dimensional engineering applications, Comput. Methods Appl. Mech. Eng. 433 (2025) 117508. https://doi.org/10.1016/j.cma.2024.117508
[59] F. Evangelista Junior, I.F. Almeida, Machine learning RBF-based surrogate models for uncertainty quantification of age and time-dependent fracture mechanics, Eng. Fract. Mech. 258 (2021) 108037. https://doi.org/10.1016/j.engfracmech.2021.108037
[60] S.S. Jin, Accelerating Gaussian process surrogate modeling using compositional kernel learning and multi-stage sampling framework, Appl. Soft Comput. 104 (2021) 106909. https://doi.org/10.1016/j.asoc.2020.106909
[61] S.H. Rudy, T.P. Sapsis, Sparse methods for automatic relevance determination, Physica D 418 (2021) 132843. https://doi.org/10.1016/j.physd.2021.132843
[62] K. Liu, Y. Li, X. Hu, M. Lucu, W.D. Widanage, Gaussian process regression with automatic relevance determination kernel for calendar aging prediction of lithium-Ion batteries, IEEE Trans. Ind. Inf. 16 (2020) 3767–3777. https://doi.org/10.1109/TII.2019.2941747
[63] Y. Deng, M. Eden, S. Cremaschi, A Gaussian process embedded feature selection method based on automatic relevance determination, Comput. Chem. Eng. 191 (2024) 108852. https://doi.org/10.1016/j.compchemeng.2024.108852
[64] J.B. Scoggins, T.J. Wignall, T. Nakamura-Zimmerer, K.L. Bibb, Multihierarchy Gaussian process models for probabilistic aerodynamic databases using uncertain nominal and off-nominal configuration data, in: AIAA SCITECH 2023 Forum, American Institute of Aeronautics and Astronautics, 2023. https://doi.org/10.2514/6.2023-1185
[65] Y.-U. Song, B.U. Song, M.-K. Jung, C. Lee, J.P. Choi, I. Lee, Multi-fidelity Gaussian process modeling of a thin-walled structure for laser powder bed fusion (LPBF) process window, J. Manuf. Process. 127 (2024) 107–114. https://doi.org/10.1016/j.jmapro.2024.07.085
[66] P. Lualdi, R. Sturm, T. Siefkes, Exploration-oriented sampling strategies for global surrogate modeling: a comparison between one-stage and adaptive methods, J. Comput. Sci. 60 (2022) 101603. https://doi.org/10.1016/j.jocs.2022.101603
[67] D.A. Cohn, Z. Ghahramani, M.I. Jordan, Active learning with statistical models, J. Artif. Intell. Res. 4 (1996) 129–145.
[68] B. Settles, Uncertainty sampling, in: Active Learning, Springer, Cham, 2012. https://doi.org/10.1007/978-3-031-01560-1_2
[69] J. Mockus, On the bayes methods for seeking the extremal point, IFAC Proceedings Volumes 8 (1975) 428–431. https://doi.org/10.1016/S1474-6670(17)67769-3
[70] D.R. Jones, M. Schonlau, W.J. Welch, Efficient global optimization of expensive black-box functions, J. Global Optim. 13 (1998) 455–492. https://doi.org/10.1023/A:1008306431147
[71] B. Shahriari, K. Swersky, Z. Wang, R.P. Adams, N. de Freitas, Taking the human out of the loop: a review of Bayesian optimization, Proc. IEEE 104 (2016) 148–175. https://doi.org/10.1109/JPROC.2015.2494218
[72] J.M. Hernández-Lobato, M.A. Gelbart, R.P. Adams, M.W. Hoffman, Z. Ghahramani, A general framework for constrained bayesian optimization using information-Based search, J. Mach. Learn. Res. 17 (2016) 5549–5601.
[73] E. Merrill, A. Fern, X. Fern, N. Dolatnia, An empirical study of Bayesian optimization: acquisition versus partition, J. Mach. Learn. Res. 22 (2021) 1–25. http://jmlr.org/papers/v22/18-220.html.
[74] J. Rodemann, T. Augustin, Imprecise Bayesian optimization, Knowl. Based Syst. 300 (2024) 112186. https://doi.org/10.1016/j.knosys.2024.112186
[75] A. Sóbester, S.J. Leary, A.J. Keane, On the design of optimization strategies based on global response surface approximation models, J. Global Optim. 33 (2005) 31–59. https://doi.org/10.1007/s10898-004-6733-1
[76] G. De Ath, R.M. Everson, A.A.M. Rahat, J.E. Fieldsend, Greed is good: exploration and exploitation trade-offs in Bayesian optimisation, ACM Trans. Evol. Learn. Optim. 1 (2021) 1. https://doi.org/10.1145/3425501
[77] V.T. Dang, C. Labergère, P. Lafon, Adaptive metamodel-assisted shape optimization for springback in metal forming processes, Int. J. Mater. Form. 12 (2019) 535–552. https://doi.org/10.1007/s12289-018-1433-4
[78] N. Srinivas, A. Krause, S.M. Kakade, M.W. Seeger, Information-Theoretic regret bounds for Gaussian process optimization in the bandit setting, IEEE Trans. Inf. Theory 58 (2012) 3250–3265. https://doi.org/10.1109/TIT.2011.2182033
[79] T. Desautels, A. Krause, J.W. Burdick, Parallelizing exploration-Exploitation tradeoffs in Gaussian process bandit optimization, J. Mach. Learn. Res. 15 (2014) 4053–4103. http://jmlr.org/papers/v15/desautels14a.html.
[80] A. Candelieri, Mastering the Exploration-Exploitation Trade-off in Bayesian Optimization, arXiv preprint arXiv:2305.08624 (2023).
[81] M. Menz, M. Munoz Zuniga, D. Sinoquet, Estimation of simulation failure set with active learning based on Gaussian process classifiers and random set theory, Struct. Saf. 117 (2025) 102607. https://doi.org/10.1016/j.strusafe.2025.102607
[82] E. Carrera, CZ0 requirements: models for the two dimensional analysis of multilayered structures, Compos. Struct. 37 (3-4) (1997) 373–383. https://doi.org/10.1016/S0263-8223(98)80005-6
[83] A.I.J. Forrester, A.J. Keane, Recent advances in surrogate-based optimization, Prog. Aerosp. Sci. 45 (2009) 50–79. https://doi.org/10.1016/j.paerosci.2008.11.001
[84] B. Peherstorfer, K. Willcox, M. Gunzburger, Survey of multifidelity methods in uncertainty propagation, inference, and optimization, SIAM Rev. 60 (2018) 550–591. https://doi.org/10.1137/16M1082469

[85] K. Ravi, V. Fediukov, F. Dietrich, T. Neckel, F. Buse, M. Bergmann, H.J. Bungartz, Multi-fidelity Gaussian process surrogate modeling for regression problems in physics, Mach. Learn. Sci. Technol. 5 (2024) 045015. https://doi.org/10.1088/2632-2153/ad7ad5
[86] D.J.J. Toal, Some considerations regarding the use of multi-fidelity Kriging in the construction of surrogate models, Struct. Multidiscip. Optim. 51 (2015) 1223–1245. https://doi.org/10.1007/s00158-014-1209-5
[87] C. Wang, Q. Duan, W. Gong, A. Ye, Z. Di, C. Miao, An evaluation of adaptive surrogate modeling based optimization with two benchmark problems, Environ. Modell. Softw. 60 (2014) 167–179. https://doi.org/10.1016/j.envsoft.2014.05.026
[88] A. Sauer, R.B. Gramacy, D. Higdon, Active learning for deep Gaussian process surrogates, Technometrics 65 (2022) 4–18. https://doi.org/10.1080/00401706.2021.2008505
[89] J.I. González, Z. Dai, P. Hennig, N.D. Lawrence, Batch Bayesian optimization via local penalization, in: International Conference on Artificial Intelligence and Statistics, 2015. https://api.semanticscholar.org/CorpusID:11897211.
[90] J.P. Folch, R.M. Lee, B. Shafei, D. Walz, C. Tsay, M. van der Wilk, R. Misener, Combining multi-fidelity modelling and asynchronous batch Bayesian optimization, Comput. Chem. Eng. 172 (2023) 108194. https://doi.org/10.1016/j.compchemeng.2023.108194
[91] L. Demasi, G. Biagini, F. Vannucci, E. Santarpia, R. Cavallaro, Equivalent single layer, zig-zag, and layer wise theories for variable angle tow composites based on the generalized unified formulation, Compos. Struct. 177 (2017) 54–79. https://doi.org/10.1016/j.compstruct.2017.06.033
[92] J.S. Tomblin, Y.C. Ng, K.S. Raju, Material qualification and equivalency for polymer matrix composite material systems, Technical Report DOT/FAA/AR-00/47, Federal Aviation Administration (FAA), 2001.
[93] O. Vallmajó, A. Arteiro, J.M. Guerrero, A.R. Melro, A. Pupurs, A. Turon, Micromechanical analysis of composite materials considering material variability and microvoids, Int. J. Mech. Sci. 263 (2024) 108781. https://doi.org/10.1016/j.ijmecsci.2023.108781
[94] J. Morris, C.J. Hansen, A.V. Amirkhizi, Improved approximation of transverse and shear stiffness for high volume fraction uniaxial composites, Mech. Mater. 129 (2019) 230–235. https://doi.org/10.1016/j.mechmat.2018.11.014
[95] J.R. Martinez, P.L. Bishay, On the stochastic first-ply failure analysis of laminated composite plates under in-plane tensile loading, Compos. Part C Open Access 4 (2021) 100102. https://doi.org/10.1016/j.jcomc.2020.100102
[96] N. Amsc, A.A. Cmps, Polymer Matrix Composites: Materials Usage, Design, and Analysis, SAE International, Warrendale, PA, USA, 2002.
[97] W.J. Jackson, R.H. Martin, An interlaminar tensile strength specimen, in: E.T. Camponeschi, Jr. (Ed.), Composite Materials: Testing and Design, Vol. 11, ASTM STP 1206, ASTM International, Philadelphia, PA, USA, 1993, pp. 333–354.
[98] S. Banerjee, B.V. Sankar, Mechanical properties of hybrid composites using finite element method based micromechanics, Compos. Part B Eng. 58 (2014) 318–327. https://doi.org/10.1016/j.compositesb.2013.10.065
[99] T. Deng, B. Gao, H. Yan, X. Chen, Q. Yang, S. Meng, In-situ mechanical property identification and delamination growth prediction of laminates, Compos. Sci. Technol. 261 (2025) 111053. https://doi.org/10.1016/j.compscitech.2025.111053
[100] P. Minigher, A. Arteiro, A. Turon, J. Fatemi, S. Guinard, L. Barrière, P.P. Camanho, On an efficient global/local stochastic methodology for accurate stress analysis, failure prediction and damage tolerance of laminated composites, Int. J. Solids Struct. 303 (2024) 113026. https://doi.org/10.1016/j.ijsolstr.2024.113026
[101] R.B. Pipes, N.J. Pagano, Interlaminar stresses in composite laminates – An approximate elasticity solution, J. Appl. Mech. 41 (3) (1974) 668–672. https://doi.org/10.1115/1.3423368
[102] A.S.D. Wang, F.W. Crossman, Some new results on edge effect in symmetric composite laminates, J. Compos. Mater. 11 (1977) 92–106. https://doi.org/10.1177/002199837701100110
[103] A. Catapano, M. Montemurro, Strength optimisation of variable angle-tow composites through a laminate-level failure criterion, J. Optim. Theory Appl. 187 (2020) 683–706. https://doi.org/10.1007/s10957-020-01750-6
[104] M. Montemurro, A. Catapano, A general B-spline surfaces theoretical framework for optimisation of variable angle-tow laminates, Compos. Struct. 209 (2019) 561–578. https://doi.org/10.1016/j.compstruct.2018.10.094
[105] M.H. Nagaraj, J. Reiner, R. Vaziri, E. Carrera, M. Petrolo, Compressive damage modeling of fiber-reinforced composite laminates using 2D higher-order layer-wise models, Compos. Part B Eng. 215 (2021) 108753. https://doi.org/10.1016/j.compositesb.2021.108753
[106] A. Pagani, A. Racionero Sánchez-Majano, M. Petrolo, Influence of structural theories on optimal fiber distributions in tow-steered composites considering local strain and stress, Aerotecnica Missili & Spazio (2025). https://doi.org/10.1007/s42496-025-00275-3
[107] K. Yoo, O. Bacarreza, M.H.F. Aliabadi, A novel multi-fidelity modelling-based framework for reliability-based design optimisation of composite structures, Eng. Comput. 38 (2022) 595–608. https://doi.org/10.1007/s00366-020-01084-x
[108] Z. Hashin, Failure criteria for unidirectional fiber composites, J. Appl. Mech. 47 (2) (1980) 329–334. https://doi.org/10.1115/1.3153664
[109] M.R. Wisnom, T. Reynolds, N. Gwilliam, Reduction in interlaminar shear strength by discrete and distributed voids, Compos. Sci. Technol. 56 (1996) 93–101. https://doi.org/10.1016/0266-3538(95)00128-X
[110] K. Senthil, A. Arockiarajan, R. Palaninathan, B. Santhosh, K.M. Usha, Defects in composite structures: its effects and prediction methods - a comprehensive review, Compos. Struct. 106 (2013) 139–149. https://doi.org/10.1016/j.compstruct.2013.06.008
[111] J.C. Brewer, P.A. Lagace, Quadratic stress criterion for initiation of delamination, J. Compos. Mater. 22 (1988) 1141–1155. https://doi.org/10.1177/002199838802201205